KCNQ2 Loss-of-Function variants disrupt neuronal maturation via early hyperexcitability followed by maladaptive network remodeling

Dirkx N.*[1,2], Kaji M.[1], De Vriendt E.[1], Carleo G.[3], Miceli F.[3], Asselbergh B.[1,2], Verstraelen P.[4], Zonnekein N.[1,2], Carotenuto L.[1], Dang L.T.[5], Sommers V.[1], Vlaemynck E.[1], Lagae L.[6], Ceulemans B.[7], De Jonghe P.[8,9], De Vos W. H.[4,10,11], Taglialatela M.[3], Weckhuysen S.[1,11,12,13]

Affiliations

1: VIB Center for Molecular Neurology, VIB, Antwerp, Belgium.

2: Department of Biomedical Sciences, University of Antwerp, Antwerp, Belgium.

3: Division of Pharmacology, Department of Neuroscience, University of Naples Federico II, Naples, Italy.

4: Laboratory of Cell Biology and Histology, University of Antwerp, Antwerp, Belgium.

5: Division of Pediatric Neurology, Department of Pediatrics, Michigan Medicine, University of Michigan, Ann Arbor, MI.

6: Department of Development and Regeneration, Paediatric Neurology, University of Leuven, Belgium. Member of European Reference Network EpiCare.

7: Department of Pediatric Neurology, University Hospital Antwerp, Antwerp, Belgium

8: Laboratory of Neuromuscular Pathology, Institute Born-Bunge, University of Antwerp, Antwerp, Belgium.

9: Neuromuscular Reference Centre, Department of Neurology, Antwerp University Hospital, Antwerp, Belgium.

10: Antwerp Centre for Advanced Microscopy, University of Antwerp, Antwerp, Belgium

11: µNeuro Research Centre of Excellence, University of Antwerp, Antwerp, Belgium.

12: Division of Neurology, University Hospital Antwerp, Antwerp, Belgium.

13: Translational Neurosciences, Faculty of Medicine and Health Science, University of Antwerp, Antwerp, Belgium.

Abstract

Loss-of-function (LOF) variants in the potassium channel subunit *KCNQ2* cause a spectrum of neonatal epilepsies from self-limiting familial neonatal epilepsy (SeLFNE) to severe developmental and epileptic encephalopathy (DEE). To dissect the developmental consequences of *KCNQ2* LOF, we conducted a longitudinal and multimodal comparative analysis in a human neuronal model generated from patients with *KCNQ2*-DEE and *KCNQ2*-SeLFNE. *KCNQ2*-LOF induced a biphasic network dysfunction, with early Kv7-driven hyperexcitability rescued by acute Retigabine (RTG) treatment, followed by maladaptive remodeling in the opposite direction. Transcriptomic analysis mirrored this biphasic dynamic trajectory, revealing an initial upregulation followed by a subsequent downregulation of synaptic genes. Structural analysis showed a steeper decline in presynaptic density alongside a distal shift in the axon initial segment (AIS) throughout maturation, and impaired AIS plasticity at later stages. Overall, KCNQ2-LOF disrupts human neuronal maturation through dynamic, biphasic changes in function, gene expression and structure, offering insights into disease mechanisms and therapeutic options.

55 **Introduction**

56 The *KCNQ2* gene encodes the Kv7.2 subunit of the voltage-gated potassium channel Kv7, which is widely
57 expressed throughout the brain (1). Kv7 channels are primarily composed of Kv7.2 and Kv7.3 subunits
58 (2). These channels are abundantly expressed at the axon initial segment (AIS), nodes of Ranvier, the
59 soma, and presynaptic terminals (3-5), where they generate the M-current, a slowly activating, non-
60 inactivating potassium current, that stabilizes membrane potential and suppresses repetitive firing (2,
61 6).

62 Human pathogenic variants in *KCNQ2* cause a spectrum of epileptic and neurodevelopmental disorders,
63 underscoring the importance of Kv7.2 in normal brain function (7-9). Most are heterozygous loss-of-
64 function (LOF) variants that reduce M-current. Dominant negative (DN) variants cause severe neonatal-
65 onset developmental and epileptic encephalopathy (*KCNQ2*-DEE) (9), while milder LOF variants cause
66 self-limited familial neonatal epilepsy (KCNQ2-SeLFNE), characterized by neonatal seizures that resolve
67 with age and typical development (8). Rare gain-of-function (GOF) variants cause developmental delay
68 with or without later onset seizures (*KCNQ2*-GOF)(7).

69 While traditional anti-seizure medication (ASM) can alleviate seizures, *KCNQ2*-DEE patients invariably
70 suffer from developmental delay. Retigabine (RTG), a selective Kv7 potassium channel opener used as
71 an ASM for focal-onset seizures, showed promise as a targeted therapy for *KCNQ2*-DEE. A retrospective
72 study involving eight *KCNQ2*-DEE patients treated with RTG reported improved developmental
73 outcomes in all patients, supporting its potential to address Kv7 dysfunction (10). Unfortunately, RTG
74 was withdrawn from the market in June 2017, mainly due to side effects related to its chemical
75 instability (11).

76 A *KCNQ2*-DEE T274M knock-in mouse model recapitulating key clinical features such as spontaneous
77 seizures and memory impairment, revealed a transient reduction in M-current and increased excitability
78 in pyramidal cells (12, 13). While mouse models provide valuable mechanistic insights, species-specific
79 differences in developmental timing and gene expression limit their translational relevance (14-17).
80 Human induced pluripotent stem cell (hiPSC)-derived neurons offer a complementary platform that
81 enables the study of patient-specific genetic variants in a human model. For instance, iPSC-derived
82 neurons with the *KCNQ2*-DEE R581Q variant exhibited accelerated action potential repolarization, larger
83 post-burst afterhyperpolarization, and dyshomeostatic enhancement of calcium activated

potassium channels (18). These findings showcase the utility of studying neuronal activity and development in a human *in vitro* setting to provide direct insight into human disease.

Given the diverse clinical phenotypes associated with *KCNQ2* variants, this study aims to provide a detailed analysis of the developmental trajectories caused by *KCNQ2*-LOF variants in a human neuronal model, through comparative transcriptomic, structural and functional profiling. To this end, we generated iPSC-derived glutamatergic cortical iNeurons of three KCNQ2-DEE patients and one KCNQ2-SeLFNE patient. We characterized these lines across early and late maturation, identifying a biphasic pattern of dysfunction: an early phase of hyperexcitability linked to direct Kv7 channel dysfunction as acute RTG treatment effectively reversed the electrophysiological alterations, followed by a later phase characterized by maladaptive changes, in which RTG exacerbated dysfunction. This biphasic trajectory was also reflected in transcriptomic and structural alterations, particularly affecting synaptic signaling. Together, our study provides new insights into the dynamic consequences of *KCNQ2*-LOF during neuronal maturation, with implications for understanding disease mechanisms and optimizing therapeutic strategies.

109

110 **Results**

111 **Generation and characterization of KCNQ2-LOF iNeurons**

112 To study *KCNQ2*-related LOF disorders, we generated iPSC-derived cortical neurons using
113 Neurogenin1/2 (NGN) overexpression (iNeurons) (Fig. 1A-B), from three patients with *KCNQ2*-DEE, each
114 carrying a *de novo* pathogenic heterozygous *KCNQ2* variant (R560W, G290D, A294V), a *KCNQ2*-SeLFNE
115 patient belonging to a two-generation pedigree carrying a segregating heterozygous variant (K327Q), a
116 healthy sibling of the *KCNQ2*-R560W patient (WT), and an isogenic control of the KCNQ2-DEE G290D
117 variant (ISO_G290D). The *KCNQ2*-DEE patients presented a typical *KCNQ2*-DEE phenotype consisting of
118 neonatal seizures and developmental delay, the SeLFNE family members exhibited neonatal seizures
119 and typical neurodevelopment (Table 1). All *KCNQ2*-DEE variants were previously reported and
120 functional studies have demonstrated a severe LOF effect (9, 19-21). All *KCNQ2* variants were classified
121 as (likely) pathogenic according to ACMG criteria (22). The *KCNQ2* variants and the correction of the
122 G290D variant were confirmed in the iPSC lines via Sanger sequencing (Fig. S1).

123

124 The expression of the short fetal and canonical *KCNQ2* transcripts (NM_172109 and NM_172107,
125 respectively) and *KCNQ3* transcript (NM_004519) were validated in iPSCs and day *in vitro* (DIV) 14
126 neurons of the control lines (WT and ISO_G290D). In line previous reports, the short fetal *KCNQ2*
127 transcript showed a decreasing expression pattern during neuronal maturation, while the canonical
128 *KCNQ2* and the *KCNQ3* transcripts showed an increase in expression levels (Fig. 1B, right) (15, 23).

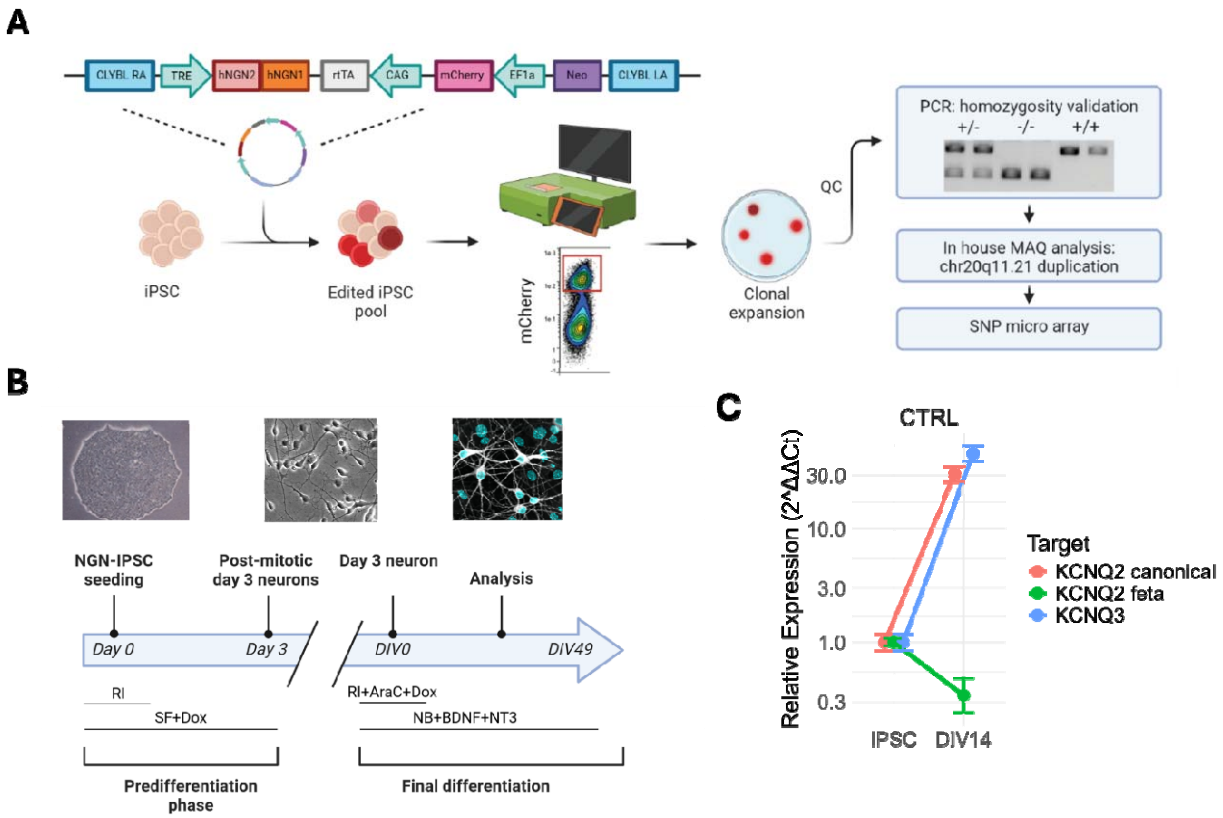

Fig. 1 Generation of and characterization of KCNQ2-LOF iNeurons. *A) Graphical overview of stable NGN-iPSC generation and quality control. B) Protocol for iNeuron generation, showing NGN-iPSC, day 3 neurons, and MAP2 positive DIV14 iNeurons. RI: Rock inhibitor, DF: Stem Flex, Dox: Doxycycline, AraC: cytosine arabinoside, NB: Neurobasal, BDNF: Brain derived neurotrophic factor, NT3: neurotrophin-3. C) RT-qPCR analysis of fetal KCNQ2, canonical KCNQ2, and KCNQ3 transcripts in iPSC and DIV14 iNeurons of pooled controls (WT and ISO_G290D). Values are normalized to respective target in iPSC lysate. N=8/4*

The KCNQ2-DEE G290D variant increases neuronal excitability under stimulation at the single-cell level

To investigate whether severe Kv7.2 LOF affects electrophysiological properties in iNeurons, we performed whole-cell patch-clamp recordings using the isogenic pair in our cohort (KCNQ2-DEE G290D and ISO_G290D), to minimize confounding effects from genetic background, between DIV 18–28. Voltage-clamp recordings showed no differences in sodium or potassium current density between lines (Fig. 2A-C). Current-clamp recordings showed that both lines were electrically active, capable of generating spontaneous action potentials (APs) at similar rates (~70% of neurons, with firing frequencies of 2.1 ± 0.5 APs/s for ISO_G290D and 2.2 ± 0.4 APs/s for G290D; Fig. 2D-E), with no significant differences in passive membrane properties (Fig2, Table 2). However, upon slow depolarizing current

146 ramps from -20 to +200 pA to assess neuronal excitability, KCNQ2-DEE G290D iNeurons fired
147 significantly more APs than ISO_G290D ($p < 0.05$; Fig. 2G–H). Single AP properties showed no differences
148 in the AP threshold, rheobase, amplitude, width, and fast afterhyperpolarization (fAHP) (Table 2). These
149 results indicate KCNQ2-DEE G290D iNeurons display increased excitability when stimulated.
150

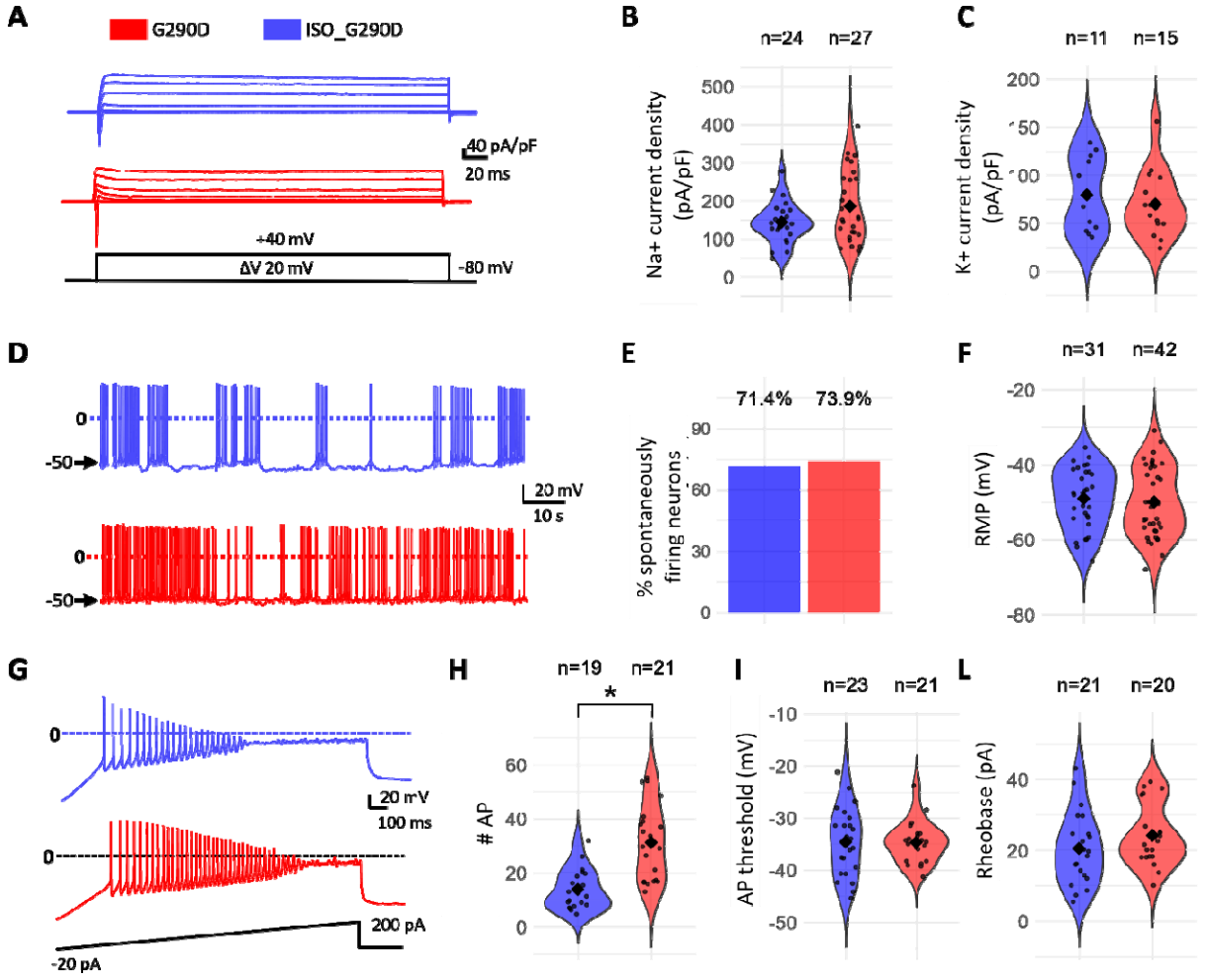

151

152 ***Fig. 2 Electrophysiological properties of KCNQ2-DEE G290D and ISO_G290D iNeurons.*** *A)*
153 *Representative current traces of KCNQ2-DEE G290D iNeurons (red) and ISO_G290D iNeurons (blue)*
154 *evoked by the indicated voltage protocol. B) Peak sodium (Na^+) current density calculated at -10 mV and*
155 *(C) potassium (K^+) current density calculated at +20mV. D) Representative traces of iNeurons*
156 *spontaneous activity recorded in whole-cell current clamp. E) Percent of spontaneously firing neurons*
157 *and (F) resting membrane potential (RMP) G) Representative current-clamp recordings during ramp*
158 *depolarization. H) Number of action potentials (APs), (I) AP threshold and (L) rheobase. In panels B, C, F,*
159 *H, I and L each bar shows the mean ± SEM from the indicated number of cells recorded in three rounds of*
160 *iNeuron differentiation (N=3). *p<0.05.*
161

KCNQ2-LOF iNeurons show earlier onset of firing and increased excitability during early maturation

To investigate the electrophysiological effects of *KCNQ2-LOF* variants on a population-wide level over time, we used high-density multielectrode arrays (HD-MEA). Neuronal cultures were recorded two to three times per week from DIV10 until DIV49. All genotypes initiated spontaneous firing between DIV10 and DIV13, with mean firing rate (MFR) and active electrode area (AA, percentage of electrodes recording spikes) significantly increasing over time ($p<0.001$, and net positive first derivatives), indicating electrophysiological maturation (Fig. S2 and Fig. S3A,B). Next, we examined whether Kv7.2 LOF affected the timing of spontaneous firing onset. During early maturation (DIV10–24), KCNQ2-LOF cultures displayed a significantly higher AA than the pooled WT and ISO_G290D ($p < 0.001$, except A294V; $p = 0.39$), suggesting that LOF neurons become electrophysiologically active earlier during maturation.

Given that all iNeuronal cultures displayed active firing by DIV13, we restricted our following analysis to recordings from this timepoint onward to ensure inclusion of active neurons across all genotypes. Throughout maturation, all genotypes demonstrated dynamic changes in electrophysiological behavior, as illustrated in the smooth functions shown in Fig. S2. Given the complexity and non-linearity of the neuronal activity changes, generalized additive models (GAM) provided a flexible and robust analytical framework to accurately characterize these effects (24). We performed pairwise comparisons between the *KCNQ2*-LOF lines and the pooled control, and generated comparative genotype-specific significance and fold change heatmaps for all parameters over time to visualize these dynamical changes (see Fig. S4 for GAM pipeline).

Comparative heatmaps revealed consistent temporal trends in neuronal activity across all KCNQ2-LOF mutant lines (Fig. 3B-C). To identify shared patterns among *KCNQ2*-LOF variants, parameters were selected based on two criteria; (i) a significant difference when comparing pooled KCNQ2-LOF vs. pooled control iNeurons (Fig. 3B), and (ii) a consistent directionality of the effect in at least three individual genotypes compared to the pooled control (Fig. 3C). All KCNQ2-LOF lines exhibited a significant increase in MFR and FR variability (coefficient of variance (CV)), particularly during early maturation, with no consistent differences in spike amplitude (Fig. 3C). Together with the patch clamp data, these results support a hyperexcitable phenotype in *KCNQ2*-LOF neurons during early maturation.

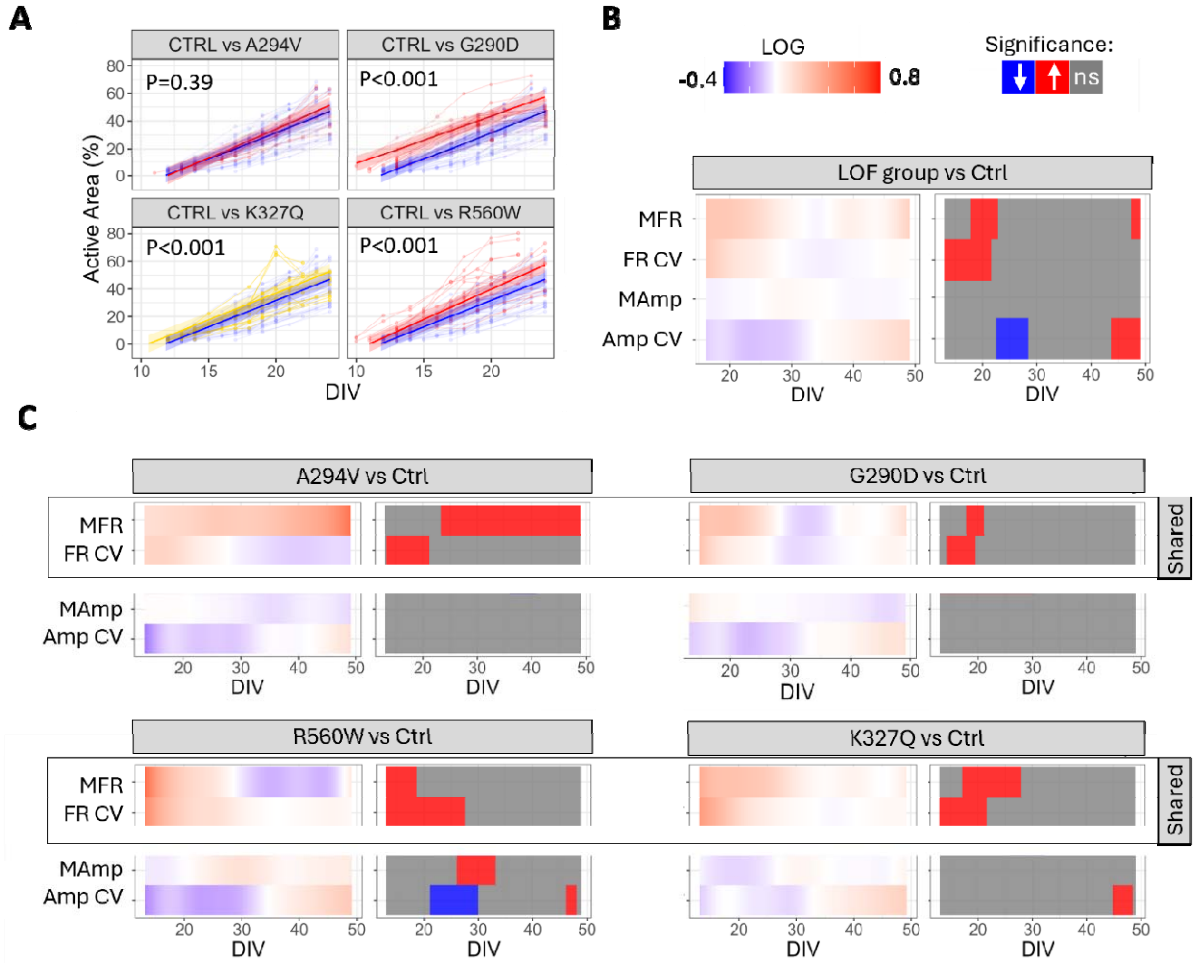

Fig. 3 Longitudinal comparison of HD-MEA activity parameters of KCNQ2-LOF iNeurons to its control. *A) Longitudinal modeling of active area percentage from DIV10–24. Thin lines show individual trajectories; solid lines show mixed-effects model predictions ±95% CI. Genotype vs. control (CTRL) comparisons used estimated marginal means with Dunnett's adjustment. Blue: CTRL; Red: KCNQ2-DEE; Yellow: KCNQ2-SeLFNE. B–C) Comparative Heatmaps show fold-change (FC) vs. CTRL; pairwise comparisons indicate significance. B) CTRL versus Grouped LOF data; C) CTRL versus Genotype-specific data. Positive FC and pairwise values (red) = increase; negative (blue) = decrease. n=39/11 CTRL, 16/6 K327Q, 13/6 A294V, 19/5 G290D, 19/7 R560W. MFR: mean firing rate; FR CV: firing rate coefficient of variance; MAmp: mean amplitude; Amp CV: amplitude coefficient of variance.*

KCNQ2-LOF iNeurons exhibit shared stable and biphasic network behavior patterns

HD-MEA network analysis revealed that all cultures developed synchronized network bursts between DIV14–21, with burst frequency (BF) increasing over time ($p<0.001$, and net positive first derivatives), reflecting neuronal maturation (25) (Fig. S3C and S5). As described by Wagenaar DA et al., our neuronal

204 cultures also exhibited an evolution in burst wave form and burst patterns throughout development
205 (26). Burst waveforms evolved from synchronous single-peak network bursts to complex synchronous
206 reverberating bursts, characterized by sequential mini-bursts occurring within a single network burst
207 (Fig. S6). Early in maturation, long-tailed network bursts were observed in ISO_G290D, G290D and
208 R560W (Fig. S7). After DIV28, long-tailed bursts were no longer observed. To accurately quantify
209 network parameters influenced by these burst tails, a 95% peak-to-baseline cut-off was applied for data
210 up to DIV28, in addition to the standard 80% cut-off used throughout the study (Table 3 and Fig. S7).
211 Due to the non-normal distribution of ISI outside of bursts, we analyzed the median as well as the 10th
212 (P10) and 90th (P90) percentiles instead of the mean.

213 Using the same inclusion criteria to define shared patterns, we identified nine parameters consistently
214 altered in *KCNQ2*-LOF lines compared to controls (Fig. 4A-B, Fig. S8). While some network parameters
215 showed a consistent increase or decrease throughout maturation, others displayed a dynamic biphasic
216 pattern with opposing trends. Dynamic parameters seemed to transition around the same DIV within
217 each genotype, allowing for the identification of two distinct phases (further named phase 1 and 2) in
218 network behavior (Fig. 4B). Throughout most of the recording period, all *KCNQ2*-LOF cultures exhibited
219 shorter inter-burst intervals (IBI), higher BF, a higher percentage of spikes occurring within bursts,
220 greater variability in spike timing within bursts (burst ISI CV), and a shorter ISI P90 outside of bursts
221 (non-burst ISI). During phase 1, these changes were accompanied by longer bursts (BD) that contained a
222 larger number of spikes (SPB), with longer ISI (burst_ISI) and greater ISI variability outside of the bursts
223 (non-burst ISI CV), which shifted in the opposite direction during phase 2 (Fig. 4, Fig. S6). The transition
224 between phases varied by line, with the SeLFNE variant K327Q transitioning almost immediately
225 (~DIV20), followed by the DEE variants R560W (~DIV30), G290D (~DIV40) and A294V (~DIV49) (Fig. 4B).

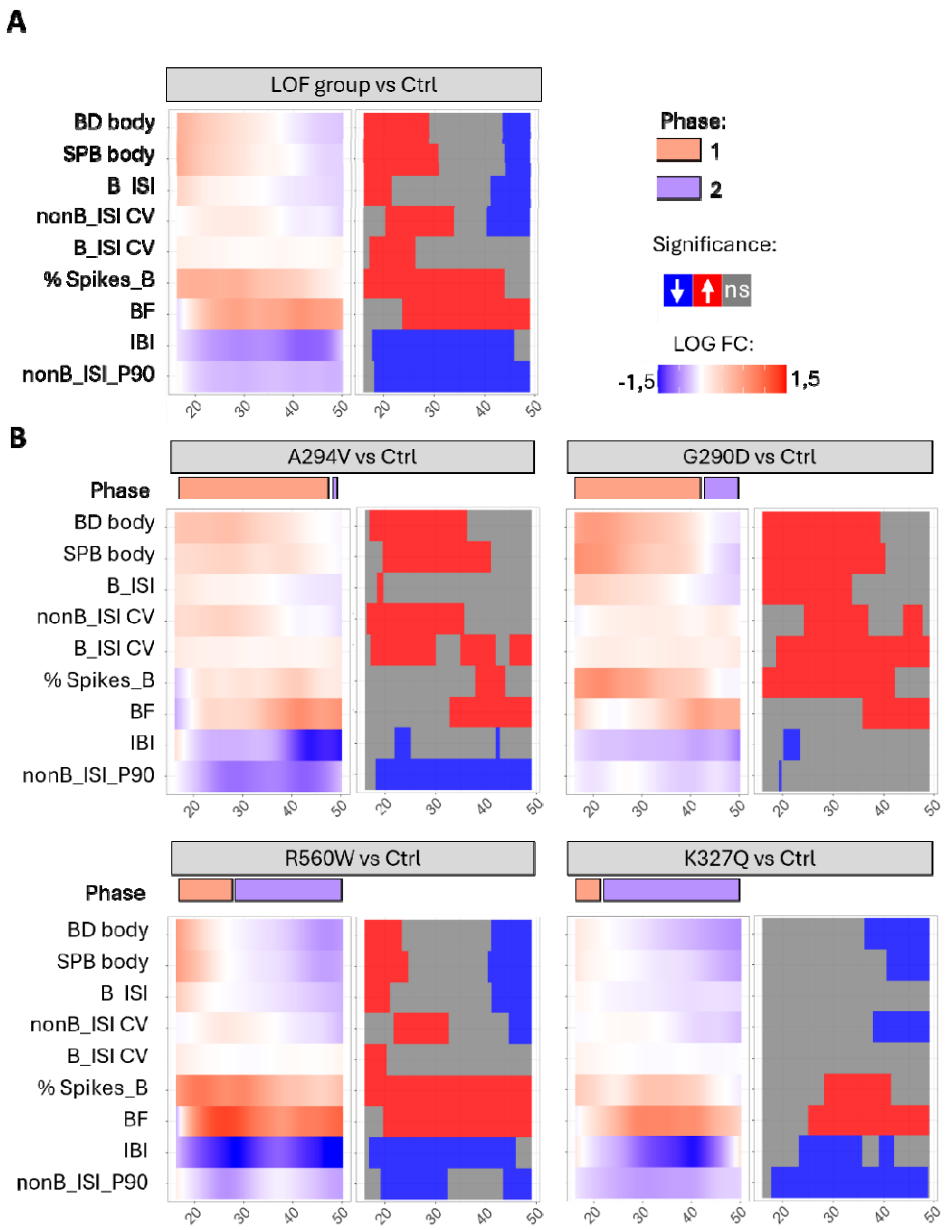

Fig. 4 Longitudinal comparison of shared HD-MEA network parameters of KCNQ2-LOF iNeurons to its control. *A) Grouped LOF data. B) Genotype-specific data. Comparative Heatmaps show fold-change (FC) vs. CTRL; pairwise comparisons indicate significance. Positive FC and pairwise values (red) = increase; negative (blue) = decrease. n=39/11 CTRL, 16/6 K327Q, 13/6 A294V, 19/5 G290D, 19/7 R560W. B: burst, BD: Burst duration, SPB: spikes per burst, ISI: interspike interval, nonB_ISI: burst inter spike interval outside of burst, CV: coefficient of variance, IBI: inter burst interval, BF: burst frequency, % spikes_B: percentage of spikes within bursts.*

237 **RTG differentially affects mutant-relevant parameters in early and late phases of neuronal maturation**
238 Given the consistent and biphasic network pattern observed in *KCNQ2*-LOF iNeurons, we used the Kv7
239 channel activator retigabine (RTG) to determine which mutant-associated parameters at phase 1 and 2
240 resulted directly from reduced M-current and which from adaptive mechanisms. First, we validated our
241 model by showing that a single 10 µM RTG exposure at DIV 21 inhibited over 80% of spontaneous firing
242 in the KCNQ2-G290D iNeurons using whole-cell patch-clamp (Fig. 5A). Second, we performed a
243 concentration-response (CR) at both phases using HD-MEA, to select a RTG concentration that affected
244 AA and burst parameters without completely silencing network bursting (all recorded wells still had to
245 show synchronized network burst activity). The AA-CR curve confirmed the silencing effectiveness of 10
246 µM RTG at phase 1 and phase 2 (Fig. 5B). Importantly, neuronal silencing by the highest RTG
247 concentration was reversible by application of 20 µM XE991, a Kv7 channel blocker (Fig. 5B),
248 demonstrating that RTG-induced silencing was not due to cell death but rather to functional modulation
249 of Kv7 channels. Interestingly, we found a nearly two-fold reduction in RTG potency during phase 2 (IC50
250 = 849 nM) compared to phase 1 (IC50 = 473 nM) (Fig. 5B). From the CR-curves, a concentration of 100
251 nM for phase 1 and 300 nM for phase 2 was selected, both approximating the IC20.

252 During phase 1, RTG but not vehicle induced network changes in G290D that pushed several phase 1
253 mutant parameters towards ISO_G290D values, notably also reducing biphasic parameters BD, SPB and
254 burst ISI (Fig. 5C-D). Additionally, RTG reduced the severity of phase-independent mutant parameters
255 non-burst ISI P90 and IBI. These results are indicative of Kv7.2 LOF playing a direct role in the phase 1
256 phenotype. In contrast, during phase 2, G290D exposure to 300 nM RTG induced similar overall effects
257 on measured parameters compared to phase 1, resulting in the rescue of the phase independent
258 network parameters, but the exacerbation of the biphasic network parameters (Fig. 5C-D).

259 These results indicate that, while decreased Kv7.2 function primarily drives the electrophysiological
260 phenotypes in phase 1, the characteristics of more mature mutant networks are partly the result of a
261 (dysfunctional) homeostatic response to the network imbalances, rather than being solely dictated by
262 Kv7.2 dysfunction.

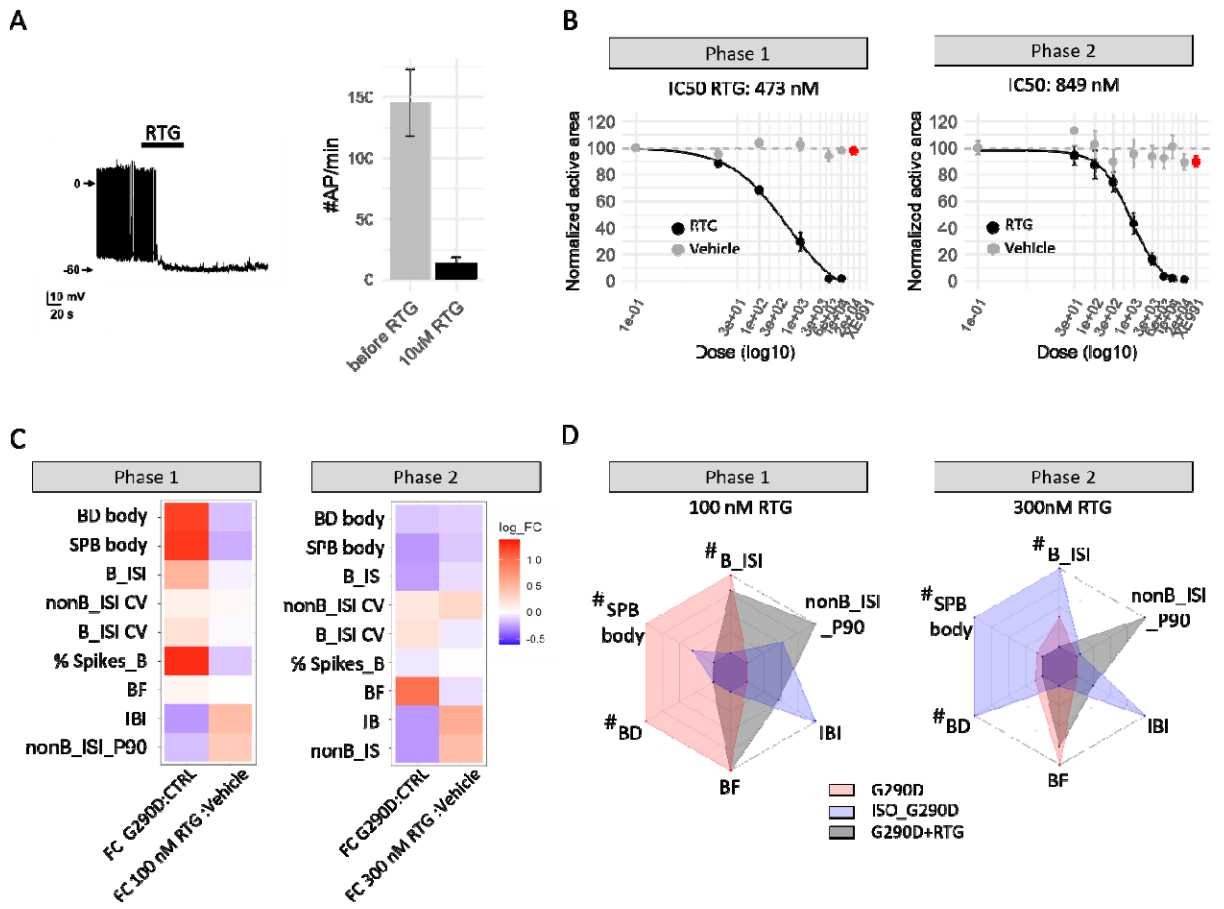

263

264 ***Fig. 5 Effect of RTG treatment on G290D during phase 1 and phase 2.*** *A) Left, Representative*
265 *spontaneous firing from whole-cell current clamp of G290D iNeurons exposure to 10 µM retigabine (RTG)*
266 *at indicated bar at DIV21. Right, barplot of mean AP per minute before and after 10 µM RTG treatment.*
267 *B) IC50 curves for RTG on G290D and XE991 (red) recovery during phase 1 and phase 2. N=9/3 for RTG,*
268 *N=7/3 for Vehicle. C) Fold change heatmap of HD-MEA network parameters comparing untreated G290D*
269 *with ISO_G290D in the first column, and the RTG-induced changes to the G290D profile in the second*
270 *column during phase 1 (Left) and 2 (Right). D) Radar maps of HD-MEA network parameters showing*
271 *G290D (pink), ISO_G290D (blue) and G290D treated with RTG (grey) at phase 1 (left) and phase 2 (right).*
272 *N=9/3 for RTG, N=7/3 for Vehicle. # indicates biphasic parameters, * indicate phase independent*
273 *parameters.*

274

275 **KCNQ2-DEE G290D Neurons Exhibit Phase-Specific Transcriptomic Dysregulation and Kv7 Channel**
276 **Expression**

To investigate transcriptomic changes underlying the biphasic network behavior, we performed RNA-seq analysis at phase 1 (DIV21) and phase 2 (DIV49) comparing KCNQ2-G290D to ISO_G290D. PCA showed clear genotype-driven separation (PC2) at both timepoints with greater divergence at DIV21 (Fig. 6A), further supported by the nearly twice as many differentially expressed genes at DIV21 compared to DIV49 (1365 vs. 723; FDR < 0.05 and |log2FC|>0.58) (Fig. S9A). Furthermore, epilepsy-associated genes were enriched at both timepoints, while cardiac disease-related gene enrichment was absent, supporting the specificity of transcriptomic changes to epilepsy-relevant pathways (Fig. S9B).

Next, we evaluated KCNQ expression in the RNA sequencing data. Both genotypes showed increasing *KCNQ2-5* expression over time (Fig. 6B). Notably, the KCNQ2:KCNQ3 expression ratio was highest at phase 1 for both genotypes and decreased substantially in phase 2 (Fig. 6C). Among the 20 highest expressed potassium channel genes, *KCNQ2* was the most highly expressed gene during both phases, with *KCNQ3* ranking second or third (Table 4). Notably, *KCNQ2* and *KCNQ3* expression was significant upregulated in G290D iNeurons at phase 1, but not phase 2 (Fig. 6B), accompanied by a shift in the KCNQ3/KCNQ2 expression ratio, from 1:4.2 (ISO_G290D) to 1:3.4 (G290D, p=0.019) (Fig. 6C). Given that Kv7.2/Kv7.3 hetero-tetramers generate an M-current density approximately 3.8 times greater than homomeric channels, these changes in gene expression likely represent an adaptive response compensating for the loss of functional M-current in G290D iNeurons.

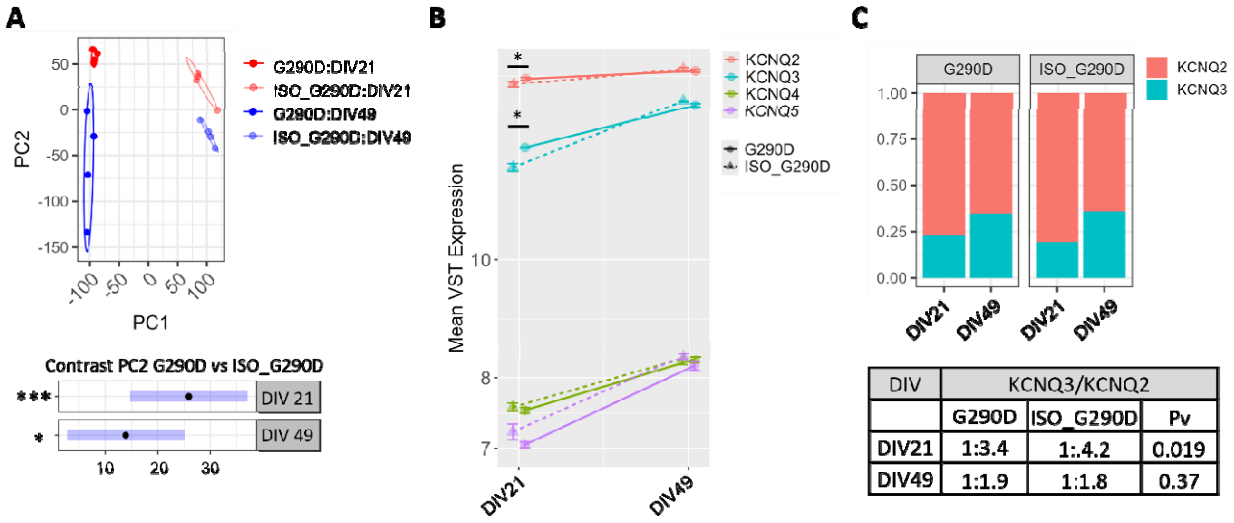

DIV	KCNQ3/KCNQ2		
	G290D	ISO_G290D	Pv
DIV21	1:3.4	1:.4.2	0.019
DIV49	1:1.9	1:1.8	0.37

Fig 6. Transcriptomic analysis of KCNQ expression in KCNQ2-G290D and ISO_G290D iNeurons in early and late maturation. *(A, top) Principal component analysis (PCA) plot of variance-stabilized expression (VST) values of all genes with non-zero variance across samples, showing separation of samples by genotype along PC2 and by time along PC1. (A, bottom) PC2 contrast calculation for DIV21 and DIV49. *p<0.05, ***p<0.001. (B) Line plots showing the mean VST expression levels + SEM of KCNQ2, KCNQ3, KCNQ4, and KCNQ5 genes over time in G290D and ISO_G290D iNeurons. (C) Proportion plots illustrating the ratio of KCNQ3 to KCNQ2 expression in G290D and ISO_G290D iNeurons at DIV21 and DIV49. The accompanying table summarizes the mean ratios and statistical comparisons between genotypes at each timepoint.*

KCNQ2-DEE G290D ineurons Display a Compensatory Shift in Potassium Channel Gene Expression during Early Maturation to Maintain Potassium Homeostasis

To explore the broader biological processes affected in developing KCNQ2-DEE G290D iNeurons, we performed gene ontology (GO) enrichment analysis on genes with significant time × genotype interaction (FDR<0.05). Enriched processes included potassium ion transport, neuron apoptotic process, dopamine transport, calcium ion import across the plasma membrane, and retrograde axonal transport (Fig. 7A). The top GO hit 'potassium ion transport' was predominantly driven by differential expression of potassium channel subunits genes and their modulators (Fig. 7B). These changes were most pronounced at phase 1, reducing or normalizing by phase 2. Notably, we observed upregulation of several genes encoding for subunits of potassium efflux channels or modulators enhancing efflux, along with downregulation of genes encoding for subunits of potassium influx channels or channel modulators reducing potassium efflux. This suggests an adaptive cellular response aimed at compensating for the loss of the Kv7.2 M-current (potassium efflux) to maintain potassium homeostasis.

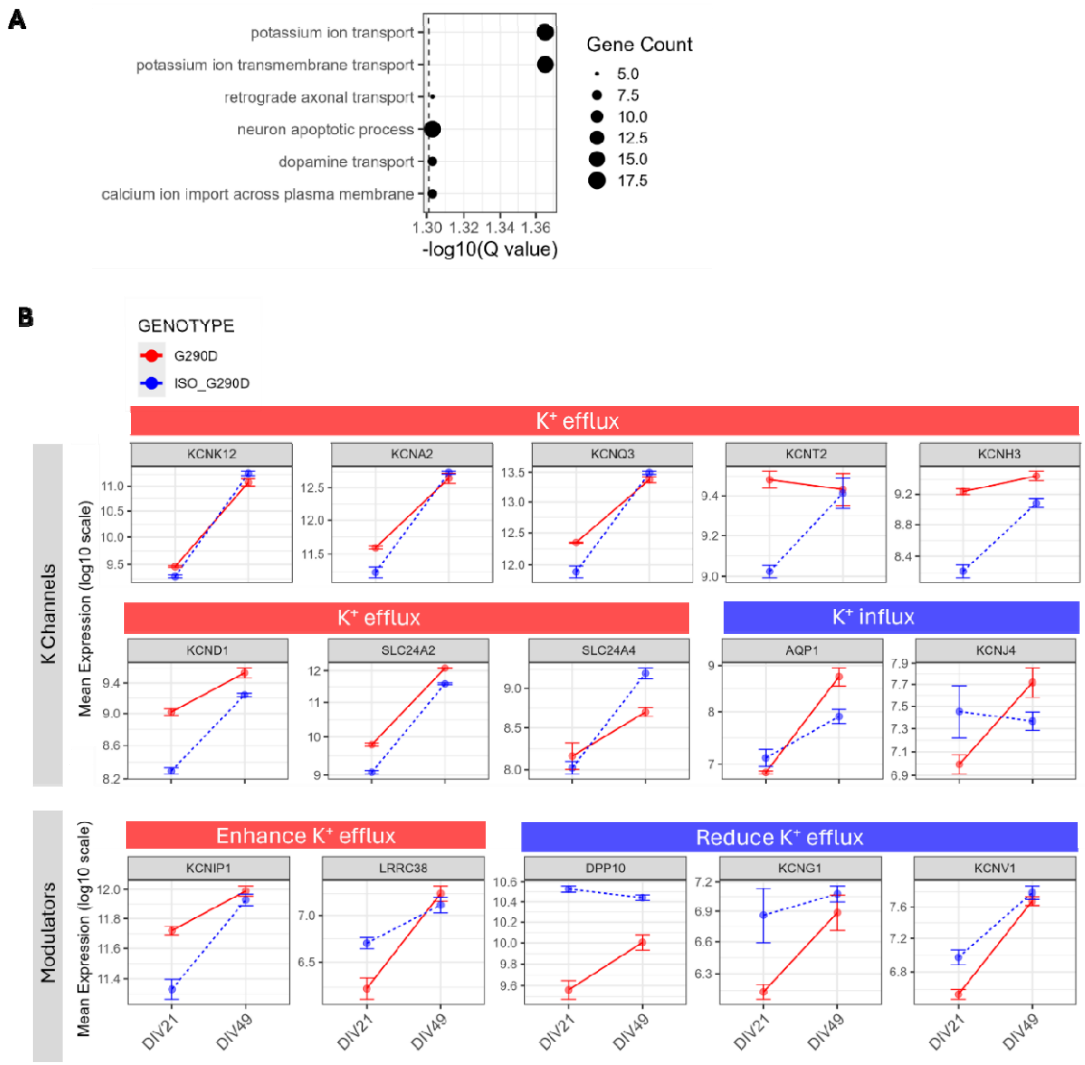

Fig 7. Transcriptional dysregulation of potassium channel gene expression in KCNQ2-DEE G290D iNeurons at early and late maturation. *(A) Gene ontology (GO) enrichment analysis of significant genes, illustrating the enriched biological processes, with a particular emphasis on potassium ion transport. (B) Line plots showing the normalized temporal expression profiles of the genes included in the potassium ion transport GO term across developmental phases. Genes encoding subunits of potassium channels are separated into subunits that are part of efflux (red) or influx (blue) potassium channels. Genes encoding for potassium channel modulators are separated into modulators that enhance (red) or reduce (blue) the efflux.*

335 **KCNQ2-DEE G290D iNeurons display phase dependent synaptic gene expression signatures aligned**
336 **with network activity changes**
337 We next performed GO enrichment analysis of biological processes at each timepoint. The top 10
338 biologically relevant GO terms were almost completely shared between timepoints and were dominated
339 by synaptic processes (Fig. S10A). Synapse specific GO term analysis (SynGO) of up- and downregulated
340 DEGs separately for each timepoint (FDR<0.05 and |log2FC|>0.58) revealed a phase-specific pattern: at
341 DIV21, synaptic enrichment was driven mainly by upregulated genes, while at DIV49 it was driven by
342 downregulated genes (Fig. S10B). Of the 49 synapse-related DEGs shared across phases, only two
343 switched direction of expression, indicating that distinct gene sets underlie the observed phase-specific
344 signatures (Fig. S10C).

345 To better understand the functional implications of these uniquely enriched up and down regulated
346 DEGs, we reviewed their reported roles in glutamatergic synaptic function (Table 5). Functional impact
347 on synaptic processes of biologically relevant DEGs is schematically summarized in Fig. 8A. In phase 1,
348 upregulated synaptic DEGs pointed to enhanced glutamate release dynamics and postsynaptic receptor
349 modulation, with overall reinforcement of excitatory synaptic stability and strength. Presynaptically, the
350 transcriptomic profile indicated enhanced recruitment, mobilization, and fusion of synaptic vesicles,
351 together with upregulation of calcium and cAMP signaling pathways, suggesting a presynaptic state
352 primed for elevated glutamatergic release. Postsynaptically, upregulation of several modulatory factors
353 enhancing NMDA and AMPA receptor signaling was observed. Since enhanced NMDA and AMPA
354 signaling is known to increase burst duration and burst frequency, respectively, we examined the
355 receptors' gene expression in the transcriptome data. This revealed a downregulation of GRIA2-4 and
356 GRIN2A, GRIN2B and GRIN3B genes, possibly reflecting a compensatory mechanism aimed at
357 dampening excessive excitatory signaling (Fig. 8B). These opposing transcriptional changes complicate
358 predictions regarding the net functional effect on NMDA and AMPA signaling.

359 Phase 2-specific downregulated synapse-related DEGs pointed towards a decreased glutamate release
360 and postsynaptic receptor modulation (Fig. 8A). Downregulation of genes associated with synaptic
361 adhesion and scaffolding suggested weakening of synaptic structure and connectivity. Presynaptically,
362 downregulated genes suggested a diminished calcium/cAMP signaling and synaptic vesicle release,
363 indicating a reduced glutamate release. Postsynaptically, a similar decrease of NMDA receptor genes
364 was observed as in phase 1, however now accompanied by downregulation of positively modulating
365 genes, suggesting decreased NMDA signaling (Fig. 8A-B), consistent with the observed shortening of BD.

366 The marked increased BF characteristic of phase 2 could reflect enhanced AMPA receptor signaling.
367 However, the transcriptomic profile was complex, with decreased AMPA receptor gene expression
368 alongside increased genes promoting AMPA receptor surface expression. To further explore other
369 postsynaptic mechanisms, we assessed small conductance calcium-activated potassium (SK) channel
370 genes (*KCNN1*-3) as reduced SK function is known to elevate burst frequency and decrease ISI (Fig. 8B-
371 C). KCNN1 was significantly downregulated, whereas KCNN3 was upregulated. As KCNN1 accounts for
372 approximately 83% of total KCNN expression at DIV49, and KCNN3 only for 8%, a net KCNN reduction
373 potentially contributes to the increased burst frequency and shortened ISI observed at phase 2 (Fig. 8C).

374 Together, these findings highlight a dynamic, biphasic regulation of synaptic gene expression in G290D
375 iNeurons, with early maturation marked by enrichment of genes promoting glutamate release, and late
376 maturation characterized by enrichment of genes associated with reduced glutamate release.

377

378

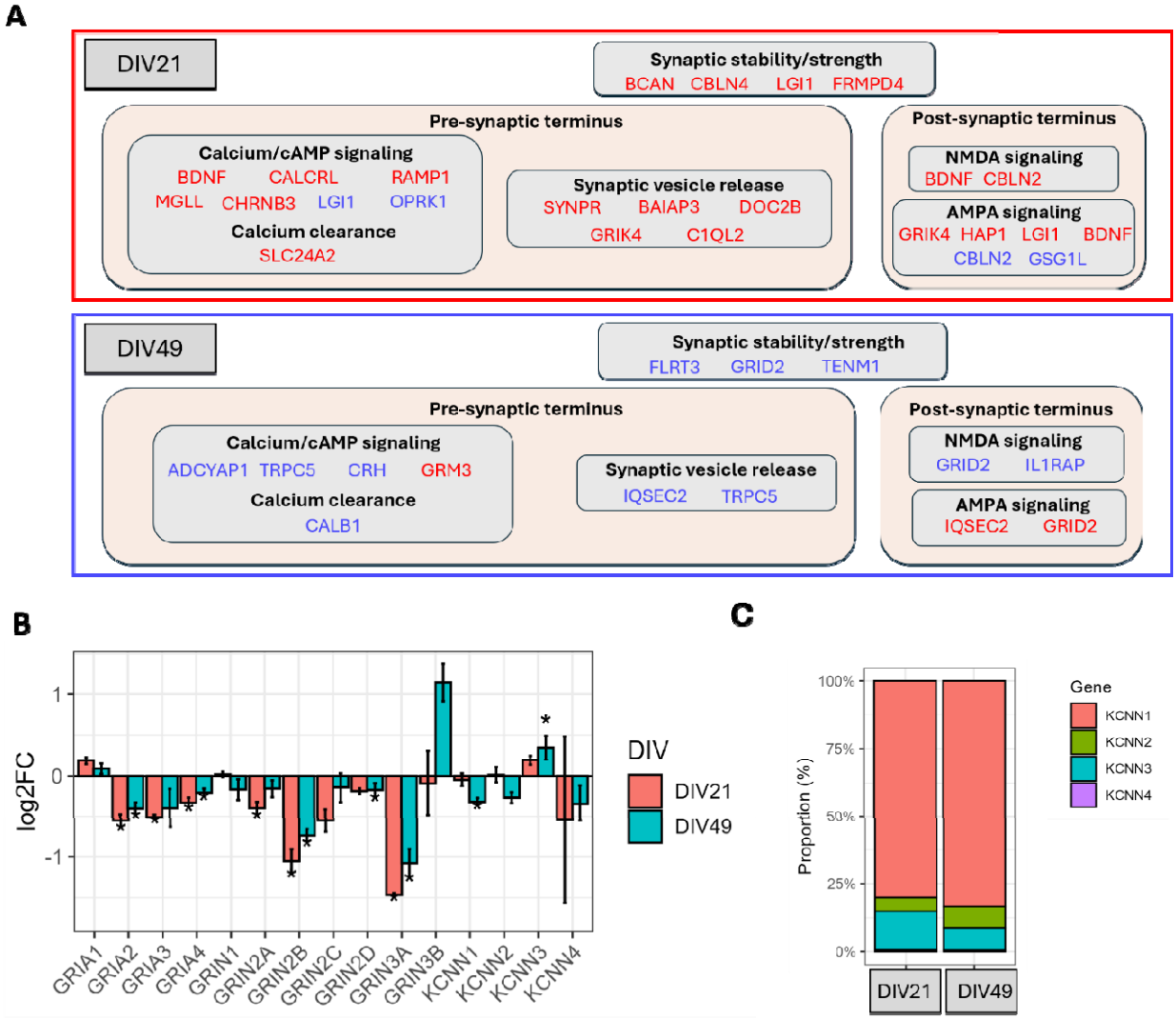

379

380 ***Fig 8. Transcriptional dysregulation of synaptic gene expression in KCNQ2-DEE G290D iNeurons in***
381 ***early and late maturation.*** *A) Schematic representation of the biologically relevant uniquely upregulated*
382 *synaptic DEGs at DIV21 (red box), and uniquely downregulated synaptic DEGs at DIV49 (blue box)*
383 *identified by SynGO term enrichment analysis and their putative roles in glutamatergic synaptic function.*
384 *DEGs are categorized according to their functional involvement in synaptic processes. DEGs highlighted*
385 *in blue are associated with a decrease in the assigned synaptic process, while DEGs in pink are associated*
386 *with an increase. B) Bar plot shows the log2 fold change in expression for AMPA/NMDA receptor*
387 *subunits genes (GRIA1-4 and GRIN1-3) and SK channel genes (KCNN1–4) in G290D mutant neurons,*
388 *compared to ISO_G290D, at DIV21 (pink) and DIV49 (blue). Data is presented as mean + SEM,*
389 **FDR<0.05. C) Proportion plots illustrating the ratio of KCNN1-4 expression in ISO_G290D neurons at*
390 *DIV21 and DIV49.*

391

392

393

394 **KCNQ2-LOF iNeurons show a greater reduction in presynaptic density over time**

395 Given the opposing trends in electrophysiological network activity and glutamatergic signaling suggested
396 from the HD-MEA and transcriptome data across maturation phases, we next assessed whether these
397 were also reflected at the synaptic structure. We quantified total pre-synaptic, post-synaptic, and
398 overall synaptic density (colocalization of Bassoon and Homer1) with MAP2 as a neurite marker (Fig. 9A).

399 At DIV21, KCNQ2-G290D and KCNQ2-R560W iNeurons showed a significant increase in pre-synaptic
400 density ($p<0.001$ and $p<0.05$, respectively), whereas KCNQ2-A294V and KCNQ2-R560W showed reduced
401 post-synaptic density ($p <0.001$ and $p<0.05$, respectively) (Fig. 9B). Only KCNQ2-G290D demonstrated an
402 increase in total synaptic density ($p<0.01$). By DIV49, a significant decrease in pre-synaptic density was
403 observed in KCNQ2-G290D alone ($p<0.001$) (Fig. 9C). However, when comparing synaptic changes over
404 time (DIV49:DIV21), all KCNQ2-LOF lines, except A294V, displayed a significantly greater reduction in
405 pre-synaptic density over time (K327Q and G290D: $p<0.001$, R560W: $p<0.01$) (Fig. 9D). The absence of a
406 significant decline in KCNQ2-A294V may reflect its delayed and still ongoing transition to phase 2.

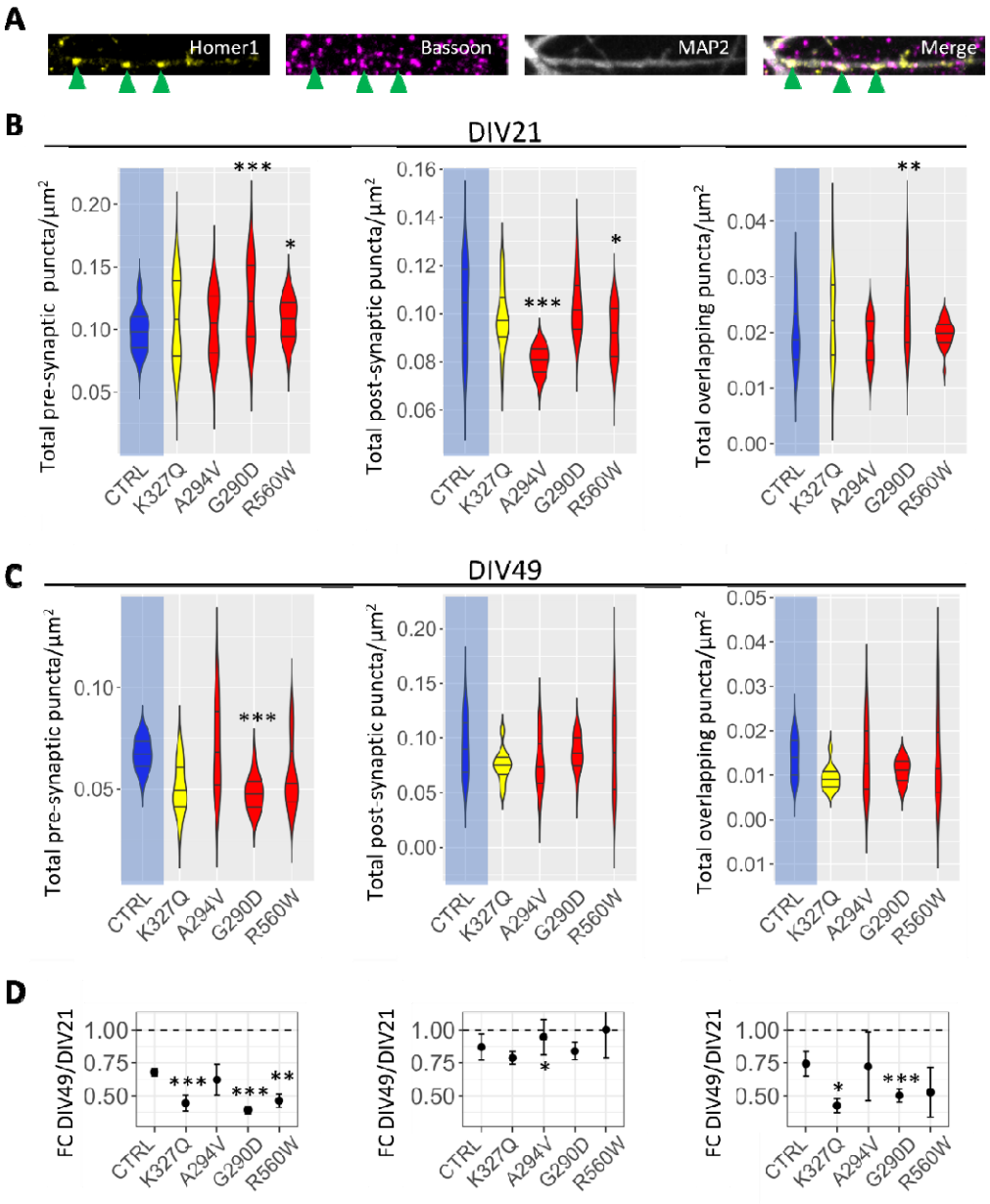

Fig9. Quantification of synaptic density across KCNQ2-LOF iNeurons at DIV21 and DIV49. *A) Representative images of dendrites at DIV21 MAP2 (dendrites, grey), Homer1 (post-synaps, Yellow) and Bassoon (pre-synaps, magenta). Green arrowheads = co-localized puncta. B, C) Quantification of total pre-, post-, and synaptic density at DIV21 (B) and DIV49 (C). Control (CTRL) in blue. D) Fold change in pre-synaptic density (DIV49:DIV21 ratio). Data represented as mean ± SEM. Statistical analysis was performed using the interaction linear mixed models, genotype x DIV ; post hoc = Benjamini-Hochberg. * p_adj < 0.05 vs. CTRL.*

417 **KCNQ2-LOF variants cause alterations in AIS Dynamics Under Naïve and Chronic Depolarizing**
418 **Conditions**

419 Kv7.2 channels interact with Ankyrin-G and are enriched at the AIS. In response to prolonged changes in
420 neuronal excitability, the AIS undergoes homeostatic structural plasticity, adjusting its length and
421 position to stabilize neuronal firing. As chronic M-current suppression in primary hippocampal neurons
422 has been shown to induce AIS structural adaptations (27), we examined whether *KCNQ2*-LOF variants
423 affect AIS length or location, using Ankyrin-G and MAP2 as markers for AIS and cell soma identification,
424 respectively. Additionally, we assessed if AIS plasticity was affected in *KCNQ2*-LOF iNeurons by the
425 established method of inducing chronic depolarization via KCl treatment at 10mM for 48 hours (Fig.
426 10A) (28-31).

427 Consistent with normal development, all genotypes showed AIS shortening and a distal-to-proximal shift
428 over time (Fig. S11) (32). Compared to the control, KCNQ2-LOF iNeurons exhibited a significant distal AIS
429 shift at both timepoints under naïve conditions, while AIS length remained unchanged in all lines except
430 for reductions in KCNQ2-G290D at DIV21, and KCNQ2-A294V at DIV49 (Fig. 10).

431 Following 48 hours of KCl treatment at DIV21, the same significant AIS differences in the *KCNQ2*-LOF
432 iNeurons compared to the control were observed as in the naïve conditions (Fig. 10B-C). Furthermore,
433 all genotypes showed AIS plasticity post KCl treatment, indicated by a KCl:Vehicle ratio significantly
434 different from one (Fig. 10B-C); AIS length decreased significantly across all genotypes ($p<0.001$) (Fig.
435 10C), and AIS position shifted further distally in the control, KCNQ2-A294V and KCNQ2-G290D ($p<0.001$,
436 $p<0.01$, $p<0.05$, respectively) (Fig. 10B). At DIV49 post KCl treatment, the distal shift in AIS location was
437 reduced for all *KCNQ2*-LOF lines compared to controls but only reached significance in the *KCNQ2*-
438 R560W and *KCNQ2*-A294V lines (Fig. 10C). Contrary to control neurons, *KCNQ2*-G290D and *KCNQ2*-
439 R560W showed a significant AIS length reduction (Fig. 10C).

440 In summary, our data show that under naïve conditions, *KCNQ2*-LOF variants cause a persistent distal
441 shift of the AIS in both early and more mature neurons. While AIS plasticity at DIV21 appears intact, DEE
442 neurons show altered plasticity at DIV49, either due to constrained AIS relocation from an already
443 distally shifted AIS or enhanced AIS shortening in response to chronic depolarization.

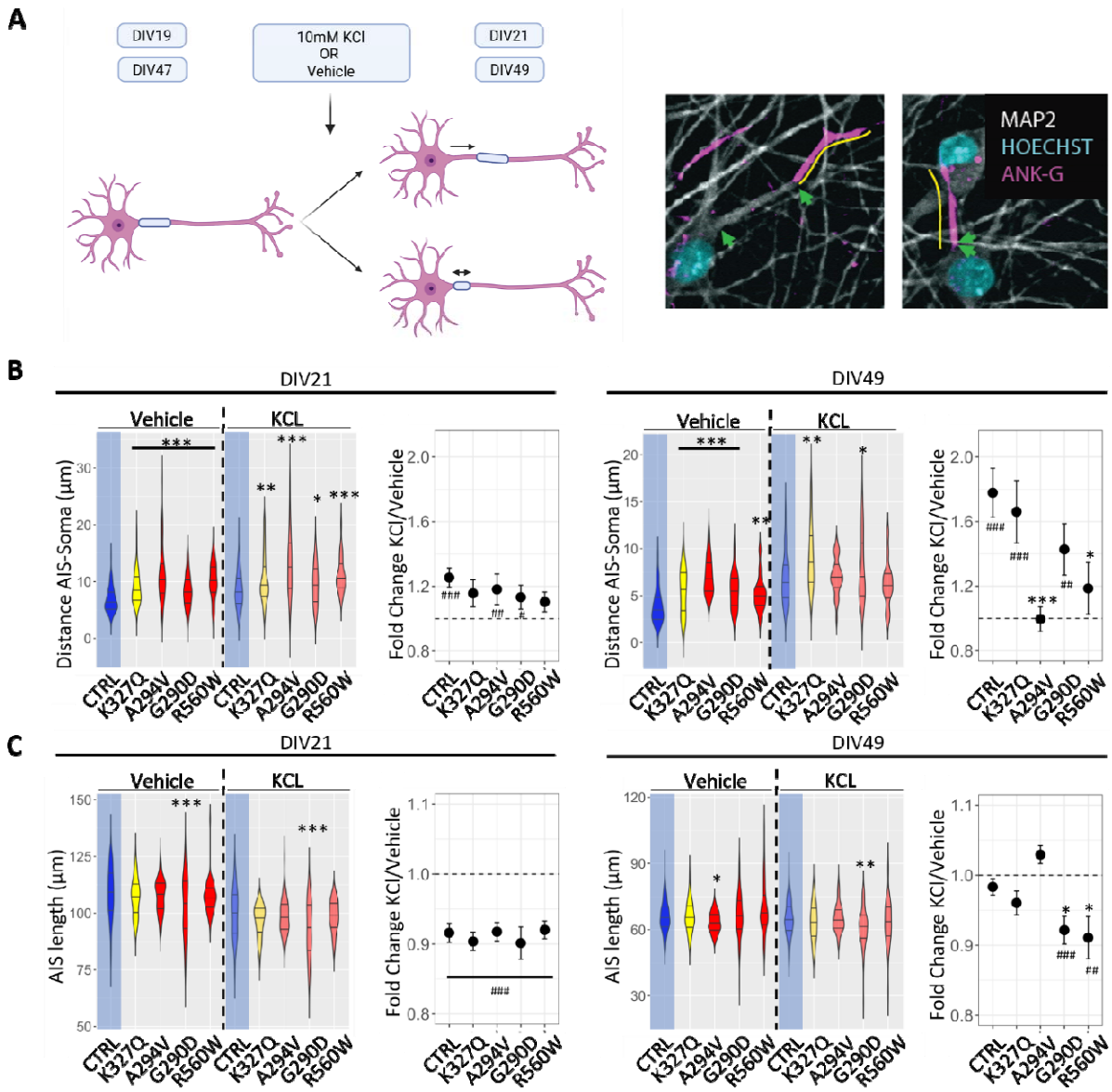

Fig10. Structural AIS modifications and plasticity in KCNQ2-LOF iNeurons. *A) Experimental overview: DIV19 and DIV47 neurons treated with 10mM KCl or vehicle for 48h; stained for AIS (AnkG, magenta), dendrites (MAP2, grey), nuclei (DAPI, cyan). Yellow line: AIS length; green arrows: soma-to-AIS start distance. B, C) Quantification of soma-to-AIS start distance (B) and AIS length (C), under vehicle and KCl conditions, and KCl/vehicle ratio, at DIV21 (left) and DIV49 (right). B) DIV21, n=48-64 pictures/genotype (756-1204 AIS/genotype, 10 wells) and DIV49, n=15-29 pictures/genotype (343-565 AIS/genotype, 10 wells). C) DIV21 n=50 pictures/genotype (6888-8367 AIS/genotype, 10 wells), DIV49 n=47-90 pictures/genotype (1951-9161 AIS/genotype, 10 wells). Data represented as mean ± SEM. Statistical analysis= GLMM with Gamma distribution and log link. post hoc = Benjamini-Hochberg. * p_adj < 0.05 vs. control (CTRL, blue); # p_adj < 0.05 vs. 1 (dashed line).*

456 **Discussion**

457 In this study, we investigated the impact of KCNQ2-LOF variants on human cortical network
458 development using glutamatergic iNeurons from individuals with KCNQ2-DEE (R560W, G290D, A294V)
459 and KCNQ2-SeLFNE (K327Q). Our longitudinal multimodal approach revealed that the pathophysiology
460 of KCNQ2-LOF in glutamatergic neurons is a dynamic process shaped by the primary loss of Kv7.2
461 function, compensatory adaptations and subsequent maladaptive changes.

462 To our knowledge, this is the first study to apply GAM to analyze longitudinal MEA data. By leveraging
463 the flexibility of GAMs, we were able to model complex, non-linear changes in neuronal network activity
464 over time, revealing a biphasic profile of network dysfunction. We first show that early in maturation,
465 KCNQ2-LOF neurons display an accelerated onset of spontaneous firing and increased excitability. At the
466 network level, KCNQ2-DEE lines also exhibited marked hyperexcitability, consistent with the findings of
467 Simkin et al., who described the functional effect of the KCNQ2-DEE R581Q variant in iNeurons. We
468 hereby validate that this is a variant-independent LOF effect (18).

469 Importantly, the most pronounced network-level differences in KCNQ2-DEE iNeurons emerged during
470 the earliest stages of network burst formation. Our transcriptome data showed an increasing
471 *KCNQ3*:*KCNQ2* expression ratio over time, aligning with previous findings that *KCNQ2* is expressed
472 earlier and at higher levels than *KCNQ3* during brain development (14-17). If this transcriptional pattern
473 translates to protein levels, it will favor the preferential formation of Kv7.2 homotetramers during early
474 maturation, making this developmental stage particularly sensitive to *KCNQ2*-LOF. Interestingly, while
475 the raster plots of Simkin et al. show minimal activity and no evidence of network bursting between
476 DIV12–DIV15, our recordings reveal the emergence of network bursts as early as DIV14. This likely
477 reflects the greater sensitivity and resolution of our HD-MEA technology, underscoring its utility in
478 detecting important early neurodevelopmental phenotypes that may be missed with conventional low-
479 density MEA.

480 We showed that these early network differences were Kv7-driven, as RTG application effectively
481 reversed these effects in KCNQ2-G290D cultures. This is further supported by prior studies showing that
482 acute pharmacological blockade of Kv7 channels in control iPSC-derived neuronal cultures induces a
483 similar hyperexcitable network phenotype to that observed in our KCNQ2-LOF lines (33, 34). At this
484 maturation stage, we observed that loss of Kv7 function altered expression of potassium channels and
485 modulators, with an overall shift toward facilitating potassium efflux, likely as a compensatory

486 mechanism to maintain potassium homeostasis. This adaptive mechanism may explain why total
487 potassium current density did not differ between *KCNQ2*-G290D iNeurons and its isogenic control
488 neurons. Additionally, all *KCNQ2*-LOF lines exhibited a distal shift in AIS positioning, mirroring effects
489 seen in rodent neurons after chronic M-current suppression (27). However, these compensatory
490 mechanisms, including relocation of the AIS and the rescue of the potassium homeostasis, appear not
491 sufficient to overcome the *KCNQ2*-LOF induced hyperexcitability.

492 As maturation progresses, network parameters in *KCNQ2*-LOF cultures exhibited a marked shift, with
493 several previously elevated metrics, such as burst duration, spikes per burst, burst ISI, falling below
494 control levels. This suggests the involvement of time-dependent compensatory and potentially
495 maladaptive mechanisms. Supporting this, RTG treatment during late maturation did not only fail to
496 normalize these biphasic parameters but exacerbated them. The absence of a similar network-level
497 transition in the study of Simkin et al. likely stems from their shorter MEA recording window (up to
498 DIV31), which precedes the critical DIV30–50 window during which our KCNQ2-DEE cultures
499 transitioned. However, Simkin et al. did report temporal changes at the single-cell level. Specifically, at
500 DIV21, KCNQ2-DEE R581Q action potential characteristics could be partially reproduced by acute Kv7
501 channel blockade in control neurons, but by DIV35, only chronic Kv7 inhibition, and not acute, mimicked
502 the disease phenotype (18). This suggests that compensatory changes emerge at the cellular level
503 before manifesting as network level alterations.

504 The biphasic pattern was also evident at the synaptic level, reflected in both transcriptional and
505 structural changes. During early maturation, synaptic GO enrichment was driven by upregulated genes
506 linked to increased presynaptic glutamate release and enhanced postsynaptic receptor activation,
507 consistent with the prolonged bursts and increased excitability observed in MEA recordings. In line with
508 this, previous studies have shown that acute pharmacological blockade of M-channels increases
509 neurotransmitter release (35, 36). In contrast, at the later maturation phase, synaptic enrichment was
510 predominantly driven by downregulated genes indicative of reduced synaptic vesicle release. Disrupted
511 synaptic vesicle recycling and reduced vesicle release have previously been linked to chronic epilepsy
512 pathophysiology (37-43). Supporting this, Birtoli and Ulrich demonstrated that shorter IBI and thus
513 increased burst frequency, can reduce the synaptic transmitter release due to insufficient recovery time
514 between bursts, thereby shortening the duration of subsequent bursts, in line with the later-stage
515 network characteristics we observed (44). Functional validation of these transcriptomic signatures in a
516 follow up study would be valuable to confirm whether the observed gene expression changes effectively

517 translate into corresponding alterations in synaptic function. This is particularly relevant as we also
518 observed structural evidence of synaptic alterations: KCNQ2-LOF lines showed a significantly steeper
519 decline in presynaptic density during maturation compared to controls.

520 Increased burst frequency is a recognized hallmark of network hyperexcitability that has been reported
521 in several other iPSC-derived epilepsy models (18, 33, 45, 46). In our KCNQ2-LOF lines, elevated burst
522 frequency may result from direct loss of Kv7, as this parameter responded favorably to RTG. However,
523 additional postsynaptic mechanisms may also contribute. Specifically, transcriptomic data revealed
524 reduced expression of the major SK channel, KCNN1, at DIV49, coinciding with reduced spikes per burst.
525 In contrast, Simkin et al. reported a maladaptive upregulation of SK channels at DIV35, a stage when
526 spikes per burst were still elevated, corresponding to the early phase of our model. This suggests that SK
527 channel expression may follow a dynamic trajectory, shifting from early compensatory upregulation to
528 later downregulation. Supporting this, Simkin et al. showed that pharmacological SK channel blockade
529 with apamin reduced spikes per bursts, mirroring the late-stage phenotype we observed.

530 Although our study includes only a single SeLFNE-line (K327Q) without an isogenic control, limiting the
531 strength of our conclusions, our findings suggest potential differences in network behavior and plasticity
532 between SeLFNE and DEE-associated *KCNQ2* variants. During early maturation, when Kv7.2 homomers
533 are likely the predominant Kv7 channel, the electrophysiological profile of the SeLFNE culture resembled
534 that of the DEE-lines but showed only subtle, largely non-significant network alterations that
535 transitioned earlier. Furthermore, when assessing activity-dependent AIS plasticity at DIV49 using
536 chronic KCl treatment, impairments were observed exclusively in the DEE lines, while the SeLFNE line
537 responded similarly to controls. Although these observations require cautious interpretation due to the
538 limited sample size and absence of isogenic controls, they support the hypothesis that more pronounced
539 early network disruptions, primarily driven by homomeric Kv7.2 homo-tetramers rather than
540 Kv7.2/Kv7.3 hetero-tetramers, may compromise the network's long-term adaptive capacity and may be
541 critical for the severity of KCNQ2-DEE. This aligns with previous work demonstrating that the current
542 density of homomeric channels in heterologous cell systems is the most reliable biophysical correlation
543 of the DEE phenotype (47). In this regard, it is relevant to note that at later neurodevelopmental stages,
544 spontaneous electrophysiological recordings no longer clearly differentiated DEE from SeLFNE cultures,
545 suggesting that spontaneous MEA profiling alone may not fully capture the neurodevelopmental deficits
546 inherent to DEE. One possibility is that these deficits in *KCNQ2*-DEE cultures may only become evident
547 under specific conditions or functional challenges, as demonstrated by our activity-dependent AIS

plasticity experiments. It is also important to consider that KCNQ2 is expressed not only in excitatory neurons but also in inhibitory neurons and astrocytes (48-50). For example, selective loss of KCNQ2 from GABAergic interneurons has been shown to increase network excitability in the immature mouse brain (51-53). Therefore, more complex *in vitro* models, such as co-culture systems incorporating inhibitory neurons and astrocytes, or organoid-based models may be necessary to distinguish DEE from SeLFNE phenotypes.

Finally, while acute RTG treatment at the late stage exacerbated several disturbed network parameters, this does not necessarily contradict the preliminary favorable clinical response to RTG seen in a small cohort of individuals with KCNQ2-DEE (10). Acute application may be insufficient to rescue long-term adaptive mechanisms, and chronic treatment of cultures is likely required to more accurately evaluate the therapeutic potential of RTG. This notion is supported by prior studies reporting differential effects of acute versus chronic RTG treatment on neuronal network behavior (54).

In summary, our longitudinal multimodal approach enabled us to map the dynamic impact of KCNQ2-LOF on cortical network development. We identified a biphasic pattern of dysfunction: an early, Kv7.2-driven hyperexcitability, followed by later maladaptive changes shaped by compensatory functional, transcriptional, and structural adaptations. Our findings highlight the importance of developmental timing in disease modeling and therapeutic testing, and underscores the value of human in vitro models for capturing the evolving nature of neurodevelopmental disease mechanisms.

Acknowledgements

All authors listed have made a substantial, direct, and intellectual contribution to the work. The authors thank the patients, control individuals and their parents who volunteered after informed consent to be sampled to generate iPSC lines for research purposes. We thank Dr. Julia Faura Llorens and Matilde Malcorps for helpful discussions regarding analysis strategies for the RNA sequencing data. We thank Professor Nael Nadif Kasri and Jack Parent for the initial training of ND in neuronal culturing techniques and for their ongoing support and advice during troubleshooting.

Author contributions

576 All authors listed have made a substantial, direct, and intellectual contribution to the work. ND, MK and
577 SW designed the experiments. ND generated all NGN-iPSC lines. ND and MK performed all the MEA
578 seedings and analysis. ND, MK, LC, NZ, EDV, VS, and EV performed the MEA recordings. ND performed
579 the imaging and transcriptome experiments. BA and PV contributed to the imaging data acquisition and
580 analysis. MK performed the pharmacological MEA experiment. GC, FM and MT designed and performed
581 the patch clamp experiments. ND, MK, GC, FM and SW wrote the manuscript. All authors revised the
582 manuscript and approved the final manuscript.

583

584 **Competing interests**

585 The authors report no competing interests.

586

587 **Funding**

588 ND receives support from FWO-SB (1S59221N). SW received support from FWO (1861419N, 1861424N,
589 G041821N), GSKE, KCNQ2 Cure Alliance, KCNQ2ev., Jack Pribaz Foundation, European Joint Programme
590 on Rare Disease JTC 2020 (TreatKCNQ). WHDV received support from BOF (ACAM core facility, 46415)
591 and FWO (I003420N, G033322N and I000123N). WHDV and PV received support from SAO-FRA
592 (20230041).

593

594 **Material and methods**

595 **Patient inclusion and generation of human induced pluripotent stem cells.**
596 Experiments involving human-derived cells were performed after informed consent and approval by the
597 Committee of Medical Ethics of Antwerp University Hospital and University of Antwerp (reference
598 19/20/257). Blood samples were taken from one proband with *KCNQ2*-SeLFNE (*KCNQ2*-K327Q), three
599 individuals with *KCNQ2*-DEE (*KCNQ2*-G290D, *KCNQ2*-A294V, and *KCNQ*-R560W), and a healthy sibling of
600 *KCNQ*-R560W (WT). The iPSC lines were generated by reprogramming subjects' PBMCs by the
601 RadboudUMC Stem Cell Technology Center (SCTC) using episomal vectors with the Yamanaka
602 transcription factors *Oct4*, c-*Myc*, *Sox2* and *Klf4* (55). As additional control line a CRISPR Cas9 corrected
603 clone of the *KCNQ2*-G290D iPSC line (ISO_G290D), generated by The Stem Cells Core Facility of the

604 Institut du Cerveau et de la Moelle Epiniere – ICM in Paris, France, was added to the cohort of this study.
605 The iPSC lines were tested for pluripotency markers (Nanog, Sox2 and Oct4) using qPCR,
606 immunohistochemistry and trilineage differentiation, and showed no abnormalities on CNV analysis.
607 Details for each iPSC lines are available in the Human pluripotent stem cell registry
608 (https://hpscreg.eu/).

609 **iPSC maintenance and stable Neurogenin (NGN)-iPSC generation**

610 The iPSCs were maintained in StemFlex medium (Thermo Fisher Scientific, A3349401) on Geltrex
611 (Thermo fisher Scientific, A1413302) coated plates at 37°C and 5% CO2. Cells were passaged using
612 ReleSR (Stemcell Technologies, 05872) when they reached 70% confluency. iPSC lines were checked for
613 mycoplasma contamination every three months.

614 Induced overexpression of human Neurogenin (hNGN) 1 and 2 was used to generate iPSC-derived
615 cortical excitatory neurons (see workflow in Fig. 1A). Stable NGN-iPSC lines were generated using two
616 TALEN plasmids (pZT-C13-R1 and pZT-C13-L1 Addgene ID: #52638 and 52637, respectively) targeting the
617 CLYBL locus to integrate a construct containing hNGN1 and hNGN2 under a doxycycline inducible
618 promoter, as well as an EF-1α promoter driving constitutive expression of mCherry (pUCM-CLYBL-
619 Ngn1/2, a gift of Dr. Michael Ward), as described by Tidball et al. 2020. In brief, iPSCs were dissociated
620 using Accutase (Sigma, A6964) and a 1E6 cell pellet was resuspended in 20 µl supplemented
621 Nucleofector solution of the P3 Primary Cell 4D-nucleofector® X Kit S (Lonza, V4XP-3032) and 2 µl of
622 plasmid mix (1:1:1, 1 µg/µl). The suspension was nucleofected with the 4D-Nucleofector Core and X Unit
623 (Lonza), using program CB-150. Ten minutes post-nucleofection, cells were plated in StemFlex media
624 supplemented with 10 µM Y-27632 rho kinase inhibitor (Tocris, 1254). iPSC lines were expanded to a
625 full 6-well plate. They were dissociated and sorted using the mCherry signal to enrich for successfully
626 engineered iPSCs. The dissociated iPSC pellet was resuspended in 1 ml FACS buffer (PBS with 2% FBS),
627 with 1000X Viability Dye eFluor® 780 (Thermo Fisher Sci., 65-0865) and incubated for 20 min on ice.
628 After incubation, 10 ml FACS buffer was added, followed by centrifugation for 3 min at 300x g to wash
629 the cells. The cell pellet was resuspended in 2 ml FACS buffer and ran through a 30 µm filter. The cell
630 suspension was added to the MACSQuant® sorting cartridge (Miltenyi Biotec). Gating hierarchies were
631 constructed using MACSQuant® Tyto software before sorting. Cell debris, doublets, and dead cells were
632 gated out. The mCherry+ sorted cells were collected from the cartridge and plated at low density to
633 generate clonal lines. 250 and 500 cells were separately seeded onto Geltrex-coated 6 well plates in

634 StemFlex media supplemented with CloneR™ (stem cell technologies, 05888). Three hours post-seeding,
635 cells were placed in an Incuctye® S3 Live Cell Analysis System and imaged every 3 hours for 7 to 10 days
636 to track colony formation from single cells. Cells were kept in CloneR supplemented media for 4 days,
637 after which the CloneR supplement was removed. Between day 7 and day 10, colonies originating from
638 single cells were picked and placed into individual wells of a 24-well plate coated with Geltrex and
639 containing StemFlex media. Clonal lines were then split into duplicate wells of a 12-well plate; one for
640 expansion and one for DNA isolation to check the zygosity of the NGN-construct. Zygosity validation was
641 performed using a multiplex of 2 primer pairs (Table 6), one targeting the CLYBL locus around the
642 insertion site, and the other within the integrated NGN-construct. All homozygous clones were checked
643 for the recurrent duplication of chr20q11.21 (15, 16) using Multiplex Amplicon Quantification (MAQ).
644 MAQ negative clones were subsequently analyzed for other CNVs using a single-nucleotide
645 polymorphism (SNP) microarray analysis.

646 **Multiplex Amplicon Quantification**

647 To exclude the presence of the recurrent duplication of chr20q11.21 (15, 16) in the corrected clonal
648 lines, we used our in-house Multiplex Amplicon Quantification (MAQ) method (Agilent). This method
649 includes multiplex PCR amplification of fluorescently labelled target and control amplicons, followed by
650 fragment analysis. The assay targets six amplicons situated in and around the chr20q11.21 region, along
651 with five control amplicons situated at random genomic positions outside the chr20q11.21 region and
652 other known CNVs. These 11 amplicons were PCR-amplified in a single reaction using 20 ng of genomic
653 DNA template. The peak areas of the target amplicons were normalized to those of the control
654 amplicons. Comparisons of the normalized peak areas between clonal lines and reference samples were
655 used to produce a dosage quotient (DQ) for each targeted amplicon, computed by the MAQ-S software
656 package (Agilent). DQ values exceeding 1.25 were considered indicative of a duplication.

657 **Generation of iPSC-derived NGN neurons**

658 NGN-iPSCs were dissociated using Accutase and 1E6 cells were seeded per well in a 6 well plate with 2
659 ml StemFlex supplemented with 10 µM Y-27632 rho kinase inhibitor (Tocris, 1254) and 2 µg/ml
660 doxycycline (Sigma, D9891). After 24 hours, 1 ml of spent media was removed and 2 ml of StemFlex
661 supplemented with 2 µg/ml doxycycline added. After 48 hours, 2 ml spent media was again removed
662 and replaced with 2 ml of StemFlex supplemented with 2 µg/ml doxycycline. 72 hours after initial
663 induction, these pre-differentiated day 3 neurons (D3N) became post-mitotic and were frozen in

664 freezing media (90% KnockOut Serum Replacement (KOS), 10% DMSO). For final differentiation, D3N
665 were co-cultured with primary mouse astrocytes in Complete Seeding media containing Neurobasal Plus
666 basal media, B27 plus (50x), BDNF (10 ng/ml), NT3 (10 ng/ml), doxycycline (2 µg/ml) (Sigma, D9891),
667 cytosine b-D-arabinofuranoside (Ara-C) and CEPT Cocktail (HY-K1043, MCE). From day 7 onwards, half-
668 media changes were performed twice a week using complete differentiation media containing
669 Neurobasal Plus basal media, B27 plus (50x), FBS (50x), BDNF (10 ng/ml) and NT3 (10 ng/ml).
670

671 **qPCR**

672 Total RNA was isolated using the Macherey-Nagel NucleoSpin RNA mini kit (Macherey-Nagel, 740955)
673 according to manufacturer's protocol. cDNA was reverse-transcribed from total RNA using the iScript
674 cDNA Synthesis Kit (Bio-Rad Laboratories, 1708890). qPCR reactions were performed in triplicate using
675 SYBR Green Real-Time PCR master mixes (Applied Biosystems, 4309155). Expression levels were
676 normalized to GAPDH and TBP, and the ΔΔCt method was used to determine the relative levels of mRNA
677 expression (56). Primers for qPCR reactions are included in table 6.
678

679 **Dissection of mouse brains and generation of primary mouse astrocyte culture**

680 All animal experiments were approved (ECD 2020-076) and conducted in accordance with the policies
681 and guidelines set forth by the Ethical Committee for Animal Testing at the University of Antwerp. These
682 policies and practices comply with European Committee Guidelines (Directive 2010/63/EU). Primary
683 mouse astrocytes were isolated from postnatal day 0-3 C57BL/6, 129/Sv and 129/Sv-KCNQ2$^{274/+}$ KI mice
684 pup brains. In brief, the cortex was isolated from the mouse brain and the meninges removed. Cortices
685 were cut into smaller pieces and dissociated in 0.25% trypsin at 37°C, 5% CO2 for 10 min. Trypsin was
686 removed and the cell suspension was resuspended 10 times in glia media (DMEM, 10% FBS, 100x
687 Glutamax, 50 U/ml P/S, 1 mM Sodium Pyruvate) supplemented with DNase I. The cell suspension was
688 incubated statically for 5 min, whereafter the supernatant, containing the single cells, was transported
689 to another conical tube. This was repeated 3 times. The cell suspension was centrifugated at 300x g for 3
690 min to remove the DNase I. The pellet was resuspended in glia media, filtered through a 0.45-micron
691 filter, and seeded on Geltrex coated T75 flasks. When confluent after approximately 5-7 days, the flask
692 was shaken vigorously for 30 seconds to remove all non-astrocyte contaminant cells Mouse astrocytes
693 of passage 2 were checked for mycoplasma and frozen in 90% FBS/10% DMSO. One week before the
694 neuronal seedings, frozen mouse astrocytes were thawed and plated in glia media on a Geltrex coated
695 T75 to allow the astrocytes to recover from the freezing process.

696 **Patch clamp recordings**

697 Whole-cell patch-clamp recording in voltage- and current-clamp configurations were performed at room
698 temperature (22-24°C) using a commercially available amplifier (Axopatch 200B, Molecular Devices).
699 Data were sampled at a frequency of 15 kHz, filtered at 5 kHz with the 4-pole low-pass Bessel filter of
700 the amplifier, and digitized using a Digidata 1440A (Molecular Devices, USA). The pCLAMP software
701 (version 10.0.2) was used for data acquisition and analysis. Recording pipettes (5-6 MΩ resistance) were
702 pulled from borosilicate glass capillaries. Solutions were applied using fast-solution exchange perfusion
703 system (CFPKGHB8, Green Leaf Scientific, Ireland). Series resistance was typically ≤ 15 MΩ, and, in most
704 recordings, compensated by at least 80%. Neurons plated on glass coverslips were continuously
705 perfused with artificial cerebrospinal fluid (aCSF) bubbled with a mixture of CO2 (5%) and O2 (95%).
706 aCSF contained (in mM): 124 NaCl, 2.5 KCl, 26 NaHCO3, 1.25 NaH2PO4, 2 MgSO4, 2.4 CaCl2, 15 glucose,
707 pH 7.35, osmolarity 305-310 mOsm. Recording pipettes were filled with standard intracellular solution
708 containing (in mM): 125 K-gluconate, 25 KCl, 10 HEPES, 10 Na2-phosphocreatine, 4 Mg-ATP, 0.4 Na 345
709 GTP, pH 7.35 adjusted with KOH; osmolality 280-290 mOsm. No correction was made for liquid junction
710 potential. Neurons meeting the following criteria were included in the analysis: holding current at -80
711 mV <100 pA, resting membrane potential (RMP) <-35 mV, series resistance < 20 MΩ, and input
712 resistance > 250 MΩ. Resting membrane potential was determined by averaging for 20 s of recording.
713 Afterward a small holding current (less than 5 pA) was used to clamp the resting membrane potential
714 close to -65 mV. Current ramps were elicited from an initial current step of -50 pA for 0.5 s followed by
715 depolarizing ramp from -50 to +200pA for 2 s. This protocol was used to calculate the action potential
716 (AP) properties as described in Simkin et al. (18)

717 **HD-MEA plate preparation and seeding**

718 Prior to cell plating, HD-MEA plates were pre-treated with 1 ml of 1% tergazyme for 1 hour, washed 3
719 times with PBS and sterilized in 70% ethanol for 30 min. After removing ethanol and washing, 1 ml of
720 Neurobasal Plus basal media with B-27 Plus supplement (50x) was added per well and incubated for 48
721 hours (37°C) to condition the chips. Afterwards, the media was removed, and the chips were washed
722 once with 1 ml PBS. The chips were coated first with 50 μl 0.14% PEI in borate buffer for 1 hour, then
723 extensively washed four times with 1 ml Milli-Q water followed by airdrying overnight. The following
724 day, the chips were coated with 20 μg/ml CellAdhere™ Laminin-521 (Stemcell Technologies, 200-0117)
725 in DMEM for 0.5 to 1 hour at 37°C. During this incubation time cell suspensions for plating were

726 prepared. Frozen D3N were thawed at 37°C in a warm water bath, and in parallel, fresh mouse
727 astrocytes of passage 2 or 3 were dissociated using 0.05% Trypsin. A mixture of 5E5 D3N and 5E4
728 astrocytes was added directly to the chips in a 50 µl cell suspension composed of Complete Seeding
729 media supplemented with Primocin (100 µg/ml) and incubated for 30 min in a 5% CO2 cell culture
730 incubator at 37 °C. After cell adherence, an additional 2 ml Complete Seeding media supplemented with
731 Primocin was gently added in the wells.

732 **HD-MEA recordings**

733 Activity and Network Assay

734 All MEA recordings were performed on a MaxTwo (MaxWell Biosystems AG, Zurich, Switzerland), using
735 MaxLab Live assays as described previously by Ronchi et al. 2020. Activity Scan Assays and Network
736 Assays were performed three times a week during critical maturation period (Monday, Wednesday,
737 Friday) from DIV12 to DIV28, and twice a week (Monday, Friday) DIV28 to DIV49 at 5% CO2 and 37°C.
738 For all the recordings, a 300 Hz high-pass filter was used and a spike detection threshold set to 5.0
739 standard deviations. For the Activity Scan Assay, the checkerboard configuration was used with a
740 recording time of 30 sec for each configuration. For the Network Assay, 1024 electrodes were selected
741 using the Maxlive neuronal selection algorithm which selects the electrodes with the highest amplitude
742 while also maximizing the distance between the individual electrodes. This reduces the potential for
743 redundant recording of the same cells with multiple electrodes and therefore increases the total
744 number of measured cells. Network measurements were recorded for 10 min. All HD-MEA media
745 changes took place immediately following recordings to allow >48 hours of media conditioning.
746 To account for the presence of long-tailed bursts until DIV28, we performed burst parameters analysis
747 using two different peak-to-baseline cut-offs, influencing the start and stop detection of the burst, for
748 data generated between DIV14 and DIV28 (Fig. 3). An 80% cut-off was used to analyze the period of
749 high-frequency spiking that defined the main body of the burst, excluding the prolonged tail which
750 results from residual network activity rather than primary bursting dynamics. A 95% cut off was used to
751 include the tail in the burst, which is particularly important for outside burst parameters including inter
752 spike interval (ISI) outside of the bursts and inter-burst interval (IBI), but also percentage spikes per
753 burst, spikes per total burst (SPB total) and total burst duration (BD total) (Table 3). For data recorded
754 after DIV28, only the 80% cut off was applied, as long-tailed bursts were no longer present, making tail
755 inclusion unnecessary.

756

757 **Pharmacological studies**

758 Acute retigabine exposure was performed either on DIV21 or between DIV53 and DIV63. Baseline
759 untreated recordings were obtained using the standard Activity and Network scan parameters as
760 described above. Concentration-response measurements were performed by adding 10 µl of retigabine
761 (10 mM stock in DMSO) or vehicle (% DMSO corresponding to equivalent exposure from associated
762 retigabine concentration), in Complete Recording media, followed by 4 min diffusion, Network scan, and
763 Activity scan, then progressing to the next ascending concentration. After reaching the maximal
764 concentration, 20 µM of the Kv7.2 channel blocker XE-991 was added to each well, followed by
765 recording as previously described. IC50 values were calculated using active area metrics normalized to
766 untreated response. Semi-log normalized data were fit to IC50 curves using GraphPad Prism.

767 **Immunostaining**

768 Neurons cultured on 96-well glass bottom plates (P96-1.5H-N, CellVis) were fixed at DIV49 using 4%
769 paraformaldehyde for 15 min. After washing with PBS, the cells were permeabilized with blocking buffer
770 (PBS, 0.1% Bovine serum albumin (Sigma B4287), 10% Goat serum, 0.1% Tween-20) supplemented with
771 0.5% Triton X-100 for 30 min. Cultures were incubated with the primary antibody overnight at 4°C in
772 blocking buffer. After two PBS washes, the cells were incubated with the secondary antibody in blocking
773 buffer for 2 hours at room temperature. Following another PBS wash, Hoechst (5000x) was added for
774 10min. After a final wash, plates were topped with 300ul PBS and sealed. Images were acquired using a
775 high-content microscope, a Nikon spinning disk confocal (Ti2 with W1 disk), using a 40X NA0.95
776 objective and standard filters for DAPI, FITC, Cy3 and Cy5. Antibodies used in this study are listed in
777 Table 7.

778 <u>AIS imaging analysis</u>

779 To assess neuronal plasticity of the AIS, neuronal cultures were treated with either 10mM KCl or Vehicle
780 for 48 hours. Two independent differentiation rounds with five wells per round for each condition were
781 stained for both DIV21 and DIV49. For a comprehensive representation of the neuronal culture, ten
782 images were taken per well. To measure the distance of the AIS to the soma, straight lines were
783 manually drawn from the start of the AIS (marked by anti-Ankyrin-G staining) to the start of the soma

784 (marked by anti-MAP2 staining) for each neuron using the line tool in ImageJ. The AIS length was
785 measured exclusively from the anti-ankyrin-G channels. Images were processed using Ilastik (version
786 1.4.0) pixel- and object-level classification to identify the AIS. Output files of ImageJ and Ilastik were
787 further processed using R for statistical analysis and graphical visualization.

788 Synaptic density analysis

789 iNeuronal cultures were stained at DIV21 and DIV49 using, pan-presynaptic marker, Bassoon,
790 glutamatergic-specific post-synaptic marker, Homer1, neurite marker, MAP2 and DNA marker, Hoechst.
791 Fifteen random Z-stacks (1 µm spacing) were acquired in each well, which originated from 2
792 independent differentiation rounds (10 wells per round). Z-projected images, for synaptic spot
793 quantification, were analyzed in FIJI, and data in R, using in house developed scripts (available from
794 https://github.com/DeVosLab/NeuroConnectivity) (57, 58). Briefly, nuclei were detected in the DAPI
795 channel using the Stardist algorithm (59), and the neurite mask was construed using the MAP2 channel.
796 Within a search area, i.e., the dilated neurite mask minus the nuclei mask, both pre- (Bassoon) and
797 postsynaptic (Homer) synaptic spots were detected using Laplacian filtering. The criterion for overlap
798 was set at least 5 overlapping pixels across both binarized images. Resulting numerical data was plotted
799 in R, with one data point representing 1 well.

800 **RNA sequencing**

801 iNeuronal cultures of four replicates per cell line were harvested at DIV21 and DIV49. RNA fraction was
802 collected using Qiazol and purified using the RNA MN kit according to the manufacturer's instructions.
803 The quality of the RNA was assessed with Fragment Analyzer 5200 (Agilent, Santa Clara, CA), using the
804 DNF-471 RNA Kit. Samples were loaded according to manufacturer instructions. RNA quality numbers
805 (RQN) values were calculated using the PROSize software (version 3.0.1.6). RQN values ranged between
806 9.7 and 10. Strand-specific transcriptome resequencing was performed by BGI (Shenzhen, China) using
807 the DNBSEQ platform with PE100. Analysis was performed in-house with a standardized pipeline
808 integrated in Genomecomb (60). The pipeline used fastq-mcf (http://code.google.com/p/ea-utils) for
809 adapter clipping. Reads were aligned to the hg38 genome reference using STAR (61) in 2-pass mode and
810 the resulting SAM file converted to CRAM format using Samtools (62). BAM files were sorted. Variants
811 were called at all positions with a totalcoverage >= 5 using both GATK HaplotypeCaller (63) and Strelka
812 (64). At the initial stage positions with a coverage < 8 or a genotype quality score < 25 were considered

813 unsequenced. Gene counts were obtained using RNA-SeQC (65) with GENCODE(66) as the reference
814 gene set.

815 **RNA sequencing analysis**

816 Differential gene expression analysis was performed using the DESeq2 package (version 1.40.2) in R.
817 Genes with fewer than 8 counts across all samples were excluded from downstream analysis. For
818 differential gene expression, count matrices and corresponding sample metadata were used to
819 construct DESeqDataSet objects in DESeq2. Three distinct experimental designs were implemented to
820 address the specific structure of each comparison using DESeqDataSetFromMatrix function. For the full
821 dataset, a multi-factor design was specified to assess the effects of genotype, time, and their
822 interaction. For individual time points, separate datasets were constructed for DIV21 and DIV49,
823 assessing the effects of genotype. Normalization and variance stabilization were performed as
824 implemented in DESeq2. Principal component analysis was performed on scaled data, with the prcomp
825 function. DEGs were identified using Benjamini-Hochberg adjusted p-value < 0.05 and absolute log2
826 fold-change ≥ 0.58 (corresponding to a fold change of 1.5). To identify biological processes significantly
827 enriched among significant genes, we performed Gene Ontology (GO) enrichment analysis using the
828 clusterProfiler package. Enrichment was adjusted using the Benjamini-Hochberg method (FDR < 0.05).
829 Synapse-specific gene set enrichment was conducted separately on downregulated and upregulated
830 DEGs at DIV21 and DIV49, using the SynGO tool (https://www.syngoportal.org). To evaluate the
831 enrichment of epilepsy-related and cardiac disease-related genes, Fisher's Exact Test was performed.
832 The epilepsy gene set was obtained from the Genes4epilepsy database (September 2024 release(67)),
833 and the cardiac disease-related gene set was sourced from the T2Diacod database
834 (t2diacod.igib.res.in/cardio). These gene sets were compared to significantly differentially expressed
835 genes identified from transcriptomic analyses. For each comparison, a 2×2 contingency table was
836 constructed to represent the overlap and exclusive members of the gene sets and the differentially
837 expressed genes. Enrichment was assessed using Fisher's Exact Test.

838 **Statistical analyses**

839 All analyses were performed in R version 4.3.0, or GraphPad Prism 10.4. In all figures, *P*-values are
840 indicated as follows: $*P < 0.05$, $**P < 0.01$, $***P < 0.001$. In each figure legend, the $n = (a)/(b)$ indicates
841 the number of wells, pictures or cells (a)/ differentiation rounds (b). All results containing only one or
842 two timepoints were analyzed using either linear mixed-effects models (LMMs) or generalized linear

843 mixed-effects models (GLMMs), depending on the distribution of the response variable. Normality of
844 residuals was tested via Shapiro–Wilk tests; LMMs (using the lmer function from the lme4 package)
845 were applied to normally distributed data, while GLMMs (using glmer) with a Gamma distribution and
846 log-link were used for positively skewed data. In both model types, fixed effects included experimental
847 group, condition (e.g., maturation stage or compound), and their interaction, while differentiation round
848 was included as a random effect to account for inter-experimental variability. Estimated marginal means
849 and pairwise contrasts were computed using the emmeans package (Lenth, 2023). Both within-group
850 and between-group contrasts were assessed depending on the experimental design. P-values were
851 obtained for all relevant comparisons and adjusted for multiple testing using the Benjamini–Hochberg
852 procedure.

853 To analyze the non-linear trends of the MEA measurement over time, we employed generalized additive
854 modeling (GAM). GAM is a flexible statistical technique that, like generalized linear models, can handle
855 incomplete observations and incorporate fixed and random effects. This approach extends traditional
856 models by allowing the fitting of non-linear relationships between predictors and the response variable,
857 making it particularly effective for accurately modeling non-linear longitudinal data. GAMs were fit to
858 each parameter of interest using the gamm4 and mgcv package in R. For each parameter, the following
859 GAM structure was used:

860 Y = parameter ~ Condition + s(div, by = Condition, k = 12, sp=0.1) + s(div, by
861 =Differentation_Round, bs = 're')

862 Condition indicates the experimental group, and the smooth term s(div) is used to capture non-linear
863 changes over time. The by term enables modelling of time-specific trends for each Condition, and
864 random smooth (e.g., bs = 're') was applied to account for random effects of differentiation round. A
865 fixed smoothing parameter (sp = 0.1) was applied to control the degree of smoothness in the time trend.

866 After generating the GAM model for each mutant line, pairwise comparisons between the smooth
867 functions of mutant and control lines were performed, along with the corresponding simultaneous
868 confidence intervals (SI) as described by Mundo et al. Regions where the SI did not cover zero were
869 considered significantly different. To improve visualization of all the parameters of the Activity Scan
870 Assay or the Network Scan Assay over time, heatmaps of the significant differences (SD) and the fold
871 changes (FC) were generated using the GAM output.

872

873 **Data availability**

874 The generated data are available from the corresponding author upon reasonable request.

875

876

877

878 **References**

879 1. Cooper EC, Harrington E, Jan YN, Jan LY. M channel KCNQ2 subunits are localized to key sites for
880 control of neuronal network oscillations and synchronization in mouse brain. J Neurosci.
881 2001;21(24):9529-40.
882 2. Wang HS, Pan Z, Shi W, Brown BS, Wymore RS, Cohen IS, et al. KCNQ2 and KCNQ3 potassium
883 channel subunits: molecular correlates of the M-channel. Science. 1998;282(5395):1890-3.
884 3. Devaux JJ, Kleopa KA, Cooper EC, Scherer SS. KCNQ2 is a nodal K+ channel. J Neurosci.
885 2004;24(5):1236-44.
886 4. Pan Z, Kao T, Horvath Z, Lemos J, Sul JY, Cranstoun SD, et al. A common ankyrin-G-based
887 mechanism retains KCNQ and NaV channels at electrically active domains of the axon. J Neurosci.
888 2006;26(10):2599-613.
889 5. Cooper EC. Made for "anchorin": Kv7.2/7.3 (KCNQ2/KCNQ3) channels and the modulation of
890 neuronal excitability in vertebrate axons. Semin Cell Dev Biol. 2011;22(2):185-92.
891 6. Brown DA, Passmore GM. Neural KCNQ (Kv7) channels. Br J Pharmacol. 2009;156(8):1185-95.
892 7. Miceli F, Soldovieri MV, Ambrosino P, De Maria M, Migliore M, Migliore R, et al. Early-Onset
893 Epileptic Encephalopathy Caused by Gain-of-Function Mutations in the Voltage Sensor of Kv7.2 and
894 Kv7.3 Potassium Channel Subunits. Journal of Neuroscience. 2015;35(9):3782-93.
895 8. Singh NA, Charlier C, Stauffer D, DuPont BR, Leach RJ, Melis R, et al. A novel potassium channel
896 gene, KCNQ2, is mutated in an inherited epilepsy of newborns. Nat Genet. 1998;18(1):25-9.
897 9. Weckhuysen S, Mandelstam S, Suls A, Audenaert D, Deconinck T, Claes LRF, et al. KCNQ2
898 encephalopathy: Emerging phenotype of a neonatal epileptic encephalopathy. Annals of Neurology.
899 2012;71(1):15-25.
900 10. Knight D, Mahida S, Kelly M, Poduri A, Olson HE. Ezogabine impacts seizures and development in
901 patients with KCNQ2 developmental and epileptic encephalopathy. Epilepsia. 2023;64(7):e143-e7.
902 11. Tompson DJ, Buraglio M, Andrews SM, Wheless JW. Adolescent Clinical Development of
903 Ezogabine/Retigabine as Adjunctive Therapy for Partial-Onset Seizures: Pharmacokinetics and
904 Tolerability. J Pediatr Pharmacol Ther. 2016;21(5):404-12.
905 12. Brun L, Viemari JC, Villard L. Mouse models of Kcnq2 dysfunction. Epilepsia. 2022;63(11):2813-
906 26.
907 13. Milh M, Roubertoux P, Biba N, Chavany J, Spiga Ghata A, Fulachier C, et al. A knock-in mouse
908 model for KCNQ2-related epileptic encephalopathy displays spontaneous generalized seizures and
909 cognitive impairment. Epilepsia. 2020;61(5):868-78.

910 14. Kanaumi T, Takashima S, Iwasaki H, Itoh M, Mitsudome A, Hirose S. Developmental changes in
911 KCNQ2 and KCNQ3 expression in human brain: possible contribution to the age-dependent etiology of
912 benign familial neonatal convulsions. Brain Dev. 2008;30(5):362-9.
913 15. Dirkx N, Miceli F, Taglialatela M, Weckhuysen S. The Role of Kv7.2 in Neurodevelopment:
914 Insights and Gaps in Our Understanding. Front Physiol. 2020;11:570588.
915 16. Smith JS, Iannotti CA, Dargis P, Christian EP, Aiyar J. Differential expression of kcnq2 splice
916 variants: implications to m current function during neuronal development. J Neurosci. 2001;21(4):1096-
917 103.
918 17. Tinel N, Lauritzen I, Chouabe C, Lazdunski M, Borsotto M. The KCNQ2 potassium channel: splice
919 variants, functional and developmental expression. Brain localization and comparison with KCNQ3. FEBS
920 Letters. 1998;438(3):171-6.
921 18. Simkin D, Marshall KA, Vanoye CG, Desai RR, Bustos BI, Piyevsky BN, et al. Dyshomeostatic
922 modulation of Ca(2+)-activated K(+) channels in a human neuronal model of KCNQ2 encephalopathy.
923 Elife. 2021;10.
924 19. Orhan G, Bock M, Schepers D, Ilina EI, Reichel SN, Loffler H, et al. Dominant-negative effects of
925 KCNQ2 mutations are associated with epileptic encephalopathy. Ann Neurol. 2014;75(3):382-94.
926 20. Vanoye CG, Desai RR, Ji Z, Adusumilli S, Jairam N, Ghabra N, et al. High-throughput evaluation of
927 epilepsy-associated KCNQ2 variants reveals functional and pharmacological heterogeneity. JCI Insight.
928 2022;7(5).
929 21. Abidi A, Devaux JJ, Molinari F, Alcaraz G, Michon FX, Sutera-Sardo J, et al. A recurrent KCNQ2
930 pore mutation causing early onset epileptic encephalopathy has a moderate effect on M current but
931 alters subcellular localization of Kv7 channels. Neurobiology of Disease. 2015;80:80-92.
932 22. Richards S, Aziz N, Bale S, Bick D, Das S, Gastier-Foster J, et al. Standards and guidelines for the
933 interpretation of sequence variants: a joint consensus recommendation of the American College of
934 Medical Genetics and Genomics and the Association for Molecular Pathology. Genet Med.
935 2015;17(5):405-24.
936 23. Rosa F, Dhingra A, Uysal B, Mendis GDC, Loeffler H, Elsen G, et al. In Vitro Differentiated Human
937 Stem Cell-Derived Neurons Reproduce Synaptic Synchronicity Arising during Neurodevelopment. Stem
938 Cell Reports. 2020;15(1):22-37.
939 24. Mundo AI, Tipton JR, Muldoon TJ. Generalized additive models to analyze nonlinear trends in
940 biomedical longitudinal data using R: Beyond repeated measures ANOVA and linear mixed models. Stat
941 Med. 2022;41(21):4266-83.
942 25. Mossink B, Verboven AHA, van Hugte EJH, Klein Gunnewiek TM, Parodi G, Linda K, et al. Human
943 neuronal networks on micro-electrode arrays are a highly robust tool to study disease-specific genotype-
944 phenotype correlations in vitro. Stem Cell Reports. 2021;16(9):2182-96.
945 26. Wagenaar DA, Pine J, Potter SM. An extremely rich repertoire of bursting patterns during the
946 development of cortical cultures. BMC Neurosci. 2006;7:11.
947 27. Lezmy J, Lipinsky M, Khrapunsky Y, Patrich E, Shalom L, Peretz A, et al. M-current inhibition
948 rapidly induces a unique CK2-dependent plasticity of the axon initial segment. Proc Natl Acad Sci U S A.
949 2017;114(47):E10234-E43.
950 28. Grubb MS, Burrone J. Activity-dependent relocation of the axon initial segment fine-tunes
951 neuronal excitability. Nature. 2010;465(7301):1070-4.
952 29. Chand AN, Galliano E, Chesters RA, Grubb MS. A distinct subtype of dopaminergic interneuron
953 displays inverted structural plasticity at the axon initial segment. J Neurosci. 2015;35(4):1573-90.
954 30. Evans MD, Dumitrescu AS, Kruijssen DLH, Taylor SE, Grubb MS. Rapid Modulation of Axon Initial
955 Segment Length Influences Repetitive Spike Firing. Cell Rep. 2015;13(6):1233-45.

956 31. Evans MD, Sammons RP, Lebron S, Dumitrescu AS, Watkins TB, Uebele VN, et al. Calcineurin
957 signaling mediates activity-dependent relocation of the axon initial segment. J Neurosci.
958 2013;33(16):6950-63.
959 32. Lindhout FW, Kooistra R, Portegies S, Herstel LJ, Stucchi R, Snoek BL, et al. Quantitative mapping
960 of transcriptome and proteome dynamics during polarization of human iPSC-derived neurons. Elife.
961 2020;9.
962 33. van Hugte EJH, Lewerissa EI, Wu KM, Scheefhals N, Parodi G, van Voorst TW, et al. SCN1A-
963 deficient excitatory neuronal networks display mutation-specific phenotypes. Brain. 2023;146(12):5153-
964 67.
965 34. Kreir M, De Bondt A, Van den Wyngaert I, Teuns G, Lu HR, Gallacher DJ. Role of Kv7.2/Kv7.3 and
966 M(1) muscarinic receptors in the regulation of neuronal excitability in hiPSC-derived neurons. Eur J
967 Pharmacol. 2019;858:172474.
968 35. Luisi R, Panza E, Barrese V, Iannotti FA, Viggiano D, Secondo A, et al. Activation of pre-synaptic
969 M-type K+ channels inhibits [3H]D-aspartate release by reducing Ca2+ entry through P/Q-type voltage-
970 gated Ca2+ channels. J Neurochem. 2009;109(1):168-81.
971 36. Martire M, Castaldo P, D'Amico M, Preziosi P, Annunziato L, Taglialatela M. M channels
972 containing KCNQ2 subunits modulate norepinephrine, aspartate, and GABA release from hippocampal
973 nerve terminals. J Neurosci. 2004;24(3):592-7.
974 37. Jiang K, Yang LT, Xue M. Breaking the Synaptic Vesicle Cycle: Mechanistic Insights into
975 Presynaptic Dysfunctions in Epilepsy. Epilepsy Curr. 2025;25(2):119-24.
976 38. Upreti C, Otero R, Partida C, Skinner F, Thakker R, Pacheco LF, et al. Altered neurotransmitter
977 release, vesicle recycling and presynaptic structure in the pilocarpine model of temporal lobe epilepsy.
978 Brain. 2012;135(Pt 3):869-85.
979 39. Scorrano G, Di Francesco L, Di Ludovico A, Chiarelli F, Matricardi S. Exploring the Landscape of
980 Pre- and Post-Synaptic Pediatric Disorders with Epilepsy: A Narrative Review on Molecular Mechanisms
981 Involved. Int J Mol Sci. 2024;25(22).
982 40. Ryan TA, Li L, Chin LS, Greengard P, Smith SJ. Synaptic vesicle recycling in synapsin I knock-out
983 mice. J Cell Biol. 1996;134(5):1219-27.
984 41. Coleman WL, Bykhovskaia M. Cooperative regulation of neurotransmitter release by Rab3a and
985 synapsin II. Mol Cell Neurosci. 2010;44(2):190-200.
986 42. Ferguson SM, Brasnjo G, Hayashi M, Wolfel M, Collesi C, Giovedi S, et al. A selective activity-
987 dependent requirement for dynamin 1 in synaptic vesicle endocytosis. Science. 2007;316(5824):570-4.
988 43. Simmons RL, Li H, Alten B, Santos MS, Jiang R, Paul B, et al. Overcoming presynaptic effects of
989 VAMP2 mutations with 4-aminopyridine treatment. Hum Mutat. 2020;41(11):1999-2011.
990 44. Cohen D, Segal M. Network bursts in hippocampal microcultures are terminated by exhaustion
991 of vesicle pools. J Neurophysiol. 2011;106(5):2314-21.
992 45. Quraishi IH, Stern S, Mangan KP, Zhang Y, Ali SR, Mercier MR, et al. An Epilepsy-Associated
993 KCNT1 Mutation Enhances Excitability of Human iPSC-Derived Neurons by Increasing Slack K(Na)
994 Currents. J Neurosci. 2019;39(37):7438-49.
995 46. Que Z, Olivero-Acosta MI, Zhang J, Eaton M, Tukker AM, Chen X, et al. Hyperexcitability and
996 Pharmacological Responsiveness of Cortical Neurons Derived from Human iPSCs Carrying Epilepsy-
997 Associated Sodium Channel Nav1.2-L1342P Genetic Variant. J Neurosci. 2021;41(49):10194-208.
998 47. Gomis-Perez C, Urrutia J, Marce-Grau A, Malo C, Lopez-Laso E, Felipe-Rucian A, et al. Homomeric
999 Kv7.2 current suppression is a common feature in KCNQ2 epileptic encephalopathy. Epilepsia.
1000 2019;60(1):139-48.
1001 48. Cooper EC, Harrington E, Jan YN, Jan LY. M channel KCNQ2 subunits are localized to key sites for
1002 control of neuronal network oscillations and synchronization in mouse brain. J Neurosci.
1003 2001;21(24):9529-40.

1004 49. Uchida T, Lossin C, Ihara Y, Deshimaru M, Yanagawa Y, Koyama S, et al. Abnormal gamma-
1005 aminobutyric acid neurotransmission in a Kcnq2 model of early onset epilepsy. Epilepsia.
1006 2017;58(8):1430-9.
1007 50. Lawrence JJ, Saraga F, Churchill JF, Statland JM, Travis KE, Skinner FK, et al. Somatodendritic
1008 Kv7/KCNQ/M channels control interspike interval in hippocampal interneurons. J Neurosci.
1009 2006;26(47):12325-38.
1010 51. Jing J, Dunbar C, Sonesra A, Chavez A, Park S, Yang R, et al. Removal of KCNQ2 from
1011 parvalbumin-expressing interneurons improves anti-seizure efficacy of retigabine. Exp Neurol.
1012 2022;355:114141.
1013 52. Soh H, Park S, Ryan K, Springer K, Maheshwari A, Tzingounis AV. Deletion of KCNQ2/3 potassium
1014 channels from PV+ interneurons leads to homeostatic potentiation of excitatory transmission. Elife.
1015 2018;7.
1016 53. Hou B, Santaniello S, Tzingounis AV. KCNQ2 channels regulate the population activity of
1017 neonatal GABAergic neurons ex vivo. Front Neurol. 2023;14:1207539.
1018 54. Bar L, Shalom L, Lezmy J, Peretz A, Attali B. Excitatory and inhibitory hippocampal neurons differ
1019 in their homeostatic adaptation to chronic M-channel modulation. Front Mol Neurosci. 2022;15:972023.
1020 55. Takahashi K, Yamanaka S. Induction of pluripotent stem cells from mouse embryonic and adult
1021 fibroblast cultures by defined factors. Cell. 2006;126(4):663-76.
1022 56. Livak KJ, Schmittgen TD. Analysis of relative gene expression data using real-time quantitative
1023 PCR and the 2(-Delta Delta C(T)) Method. Methods. 2001;25(4):402-8.
1024 57. Verstraelen P, Verschuuren M, De Vos WH. Integrated staging of morphofunctional connectivity
1025 in neuronal cultures. STAR Protoc. 2024;5(2):102957.
1026 58. Verstraelen P, Garcia-Diaz Barriga G, Verschuuren M, Asselbergh B, Nuydens R, Larsen PH, et al.
1027 Systematic Quantification of Synapses in Primary Neuronal Culture. iScience. 2020;23(9):101542.
1028 59. Schmidt U, Weigert M, Broaddus C, Myers G, editors. Cell Detection with Star-Convex Polygons.
1029 Medical Image Computing and Computer Assisted Intervention – MICCAI 2018; 2018 2018//; Cham:
1030 Springer International Publishing.
1031 60. Reumers J, De Rijk P, Zhao H, Liekens A, Smeets D, Cleary J, et al. Optimized filtering reduces the
1032 error rate in detecting genomic variants by short-read sequencing. Nat Biotechnol. 2011;30(1):61-8.
1033 61. Dobin A, Davis CA, Schlesinger F, Drenkow J, Zaleski C, Jha S, et al. STAR: ultrafast universal RNA-
1034 seq aligner. Bioinformatics. 2013;29(1):15-21.
1035 62. Li H, Handsaker B, Wysoker A, Fennell T, Ruan J, Homer N, et al. The Sequence Alignment/Map
1036 format and SAMtools. Bioinformatics. 2009;25(16):2078-9.
1037 63. DePristo MA, Banks E, Poplin R, Garimella KV, Maguire JR, Hartl C, et al. A framework for
1038 variation discovery and genotyping using next-generation DNA sequencing data. Nat Genet.
1039 2011;43(5):491-8.
1040 64. Kim S, Scheffler K, Halpern AL, Bekritsky MA, Noh E, Kallberg M, et al. Strelka2: fast and accurate
1041 calling of germline and somatic variants. Nat Methods. 2018;15(8):591-4.
1042 65. Graubert A, Aguet F, Ravi A, Ardlie KG, Getz G. RNA-SeQC 2: efficient RNA-seq quality control
1043 and quantification for large cohorts. Bioinformatics. 2021;37(18):3048-50.
1044 66. Mudge JM, Carbonell-Sala S, Diekhans M, Martinez JG, Hunt T, Jungreis I, et al. GENCODE 2025:
1045 reference gene annotation for human and mouse. Nucleic Acids Res. 2025;53(D1):D966-D75.
1046 67. Oliver KL, Scheffer IE, Bennett MF, Grinton BE, Bahlo M, Berkovic SF. Genes4Epilepsy: An
1047 epilepsy gene resource. Epilepsia. 2023;64(5):1368-75.

1048

1049